PHOSPHATE BASED PROOF OF CONCEPT FOR A MICROFLUIDIC MULTI-NUTRIENT IN-SITU AUTO-ANALYZER

A THESIS SUBMITTED TO THE GRADUATE DIVISION OF THE UNIVERSITY OF HAWAIʻI AT MĀNOA IN PARTIAL FULFILLMENT OF THE REQUIREMENTS FOR THE DEGREE OF

MASTER OF SCIENCE
in
OCEANOGRAPHY

DECEMBER 2020

By
Nathaniel D. Harmon

Thesis Committee:

Christopher Sabine, Chairperson
Mariko Hatta
Christopher Measures

Keywords: Phosphate, In-Situ, Auto-Analyzer, Sequential Injection

Dedication

This work is primarily dedicated to my mother Erica, father James, brother Wesley, sister Amelia, and spouse Kristen without whom this would never have come to fruition. In addition, the support received from Gabrielle Weiss was instrumental in overcoming the situation we found ourselves in. To Dr. Hatta and Dr. Ruzicka, thank you for lending an ear to help me develop ideas into reality, even that bad ones. Finally, I would like to express my deepest gratitude to Dr. Sabine for stepping in and providing the mentorship and guidance that I always wanted from an advisor.

Abstract

Progress and discovery in the understanding and modeling of biogeochemical processes in natural waters has been limited by our ability to make measurements at relevant spatial and temporal scales. Innovations in microfluidics have led to the miniaturization of traditional reagent-based assays without loss in sensitivity. Micro Sequential Injection Analysis (μSIA) represents the second generation of flow injection analysis (FIA) techniques and solved many of the problems inherent to Continuous Flow Analysis (CFA) and first generation of FIA. The μSIA system comprises (one or two) high precision pump (s), holding coil(s), a multi-channel Lab-on-Valve (LoV) module with an external flow cell, a light source and a spectrophotometer. All components are fully computer controlled, and by using these high precision pumps and the capability of the discontinuous bi-directional flow one can obtain reproducible results. The high precision pumps not only allow for control of the mixing between small volumes of sample and reagents for each analysis but also a low standard deviation of the determinations, which then leads to nanomolar level of the detection limits (Hatta et al., 2018; Hatta el al., 2019; Ruzicka et al., 2019). The greatest advantage of the μSIA platform comes from its ability to perform any spectrophotometric, fluorometric, or chemiluminescence assay without any major reconstruction of the system simply by using a programmed sequence for each method using appropriate reagents. All of these advantages make it an ideal platform for in-situ autonomous applications. To this effect the objective of this work is to design and deploy an autonomous field deployable μSIA system using phosphate as a proof of concept

to demonstrate the viability of this equipment for further development introducing multiple assays on the same system.

Achieving the objective of this work required development and adaptation of the chemical analytical methodology and the development of an electrical control system and a housing system to deploy it. Through experimentation it was found that traditional phosphate methodology required optimization for use in an autonomous system. Thus, presented here are two viable versions of a phosphate based single-pump μSIA chemical assay adapted from recent publications in programable flow injection methods (Hatta el al., 2019; Ruzicka et al., 2019). The first assay uses sulfuric acid (H_2SO_4) as a source of protons to the reaction while the second utilizes hydrochloric acid (HCl), and both incorporate the surfactant sodium dodecyl sulfate. The H_2SO_4 based assay requires a 600sec reaction time, achieves a limit of detection of 45nM P, and is unaffected by changes in salinity. The HCl based method has a reaction time of 50sec or 100sec in fresh and sea water respectively and a limit of detection of 14nM PO_4. Due to the difference in reaction times between fresh and sea water the HCl method is subject to a salinity matrix effect. The matrix effect observed in the HCl based method may be overcome by comparing the slopes of the reaction curve as opposed to the absorbance, though more study is needed to verify this. In order to build the new autonomous platform a control scheme was developed to facilitate communication and distribute power to the different components using a Raspberry Pi single board computer. A new protocol sequence was developed using the python programing language to perform the assay and clean the μSIA manifold. Two housing systems were developed for use in dockside and submerged environments. Using the dockside housing numerous laboratory-based experiments were conducted to optimize the

chemistry of the phosphate assay for continuous determination. Two deployments (dockside and reef) and submergence tests were conducted to evaluate the capability of the autonomous platform. The successful dockside deployment was conducted in the Hawaii Kai marine embayment located on the south-east coast of the island Oahu, Hawaii USA, using the H_2SO_4 method over the course of 3 days. Unfortunately, the reef deployment was unsuccessful and resulted in loss of equipment. Despite the loss of equipment, this work achieves its objectives in providing a proof of concept for a microfluidic multi-nutrient in-situ auto-analyzer.

TABLE OF CONTENTS

LIST OF TABLES

LIST OF FIGURES

LIST OF ABBREVIATIONS

Acronym	*Definition*
AA	Ascorbic Acid Reagent
ADP	Adenosine Diphosphate
AMo	Ammonium Molybdate Tetrahydrate
ATP	Adenosine Triphosphate
Brij	Polyethylene Glycol Dodecyl Ether
DI	Deionized Water
DNA	Deoxyribonucleic Acid
FIA	Flow Injection Analysis
GPIO	General Purpose Input Output
H_2SO_4	Sulfuric Acid
HCl	Hydrochloric Acid
KSb	Potassium Antimony Stock Solution
LNSW	Low Nutrient Sea Water
LOD	Limit of Detection
LoV	Lab on Valve
MO	Mixed Molybdate Reagent
MPA	12-Molybdophosphoric Acid
MPV	Multi Position Valve
pFI	Programable Flow Injection
PMoB	Phosphomolybdenum Blue
RNA	Ribonucleic Acid
Sb-PMoB	Antimony(III) 12-Molybdophosphoric Acid
SDS	Sodium Dodecyl Sulfate
SFC	Stop in Flow Cell Protocol
SHC	Stop in Holding Coil Protocol
SOEST	School of Ocean and Earth Sciences and Technology
SW	Sea Water
UHM	University of Hawaii Manoa
USB	Universal Serial Bus
µSIA	Micro Sequential Injection Analysis

Chapter 1. Introduction

Progress and discovery in the understanding and modeling of biogeochemical processes in natural waters has been limited by our ability to make measurements at relevant spatial and temporal scales. To this effect, the goal of this thesis is to design and deploy an autonomous field deployable Micro Sequential Injection Analysis (μSIA) system using phosphate as a proof of concept. Demonstrating the viability of the phosphate assay will catalyze further development e.g., including multiple assays on the same instrument. This work is organized into four chapters. The first chapter provides an introduction into phosphate and the current methods for making determinations in aqueous solutions. The second chapter is dedicated to a presentation of the μSIA method chemistry. In total three new single pump phosphate μSIA methodologies are presented, with two being recommended for further study. Chapter three provides the design specifications of the field deployable μSIA system. The field deployable μSIA system consists of the μSIA manifold, the control and power systems, the protocol sequence, and the design of the housing and mounting systems developed for this work. The final chapter is the presentation of the results. The results include lab-based testing of environmental variables, deployments, discussion of the experimental results and the project as a whole and concludes with recommendations for future development.

1.1 Properties of Phosphorus

Phosphorus (P) is a group 15 member with nitrogen, arsenic, antimony, and bismuth, has an the atomic number 15, and is pentavalent. P can exist in oxidation states ranging from -3 to +5 with -3, +3, and +5 being the most important (Kirby & Warren, 1967).

Phosphorus(V) is by far the most common oxidative state of P, with orthophosphate (PO_4^{3-}) being the most important P compound in the natural world.

1.2 Properties of Phosphate

Orthophosphate has a molar mass of 94.97 g/mol and is arranged in a tetrahedral geometry with four oxygen atoms bonded (one double and 3 single bonds) to the central P atom. The phosphate ion has three conjugate acids hydrogen phosphate (HPO_4^{2-}), dihydrogen phosphate ($H_2PO_4^{1-}$), and phosphoric acid (H_3PO_4). The phosphate unit can be found as an ester attached to a hydrocarbon (organic phosphate) or as a salt of phosphoric acid (inorganic phosphate).

Phosphate (PO_4^{3-}) is an essential macronutrient used by all taxonomic classifications of life (Hecky & Kilham, 1988). PO_4 use by biological organisms is ubiquitous including use in the functional groups of the phospholipid molecules in the plasma membrane (Lamond, 2002). Dephosphorylation of adenosine triphosphate (ATP) and adenosine diphosphate (ADP) represent the bioenergetic processes that power cellular functions (Elser, 2012). Deoxyadenosine monophosphate forms the phosphodiester covalent bonds between the deoxyribose molecules of 2 nucleotides in DNA and RNA. As such, the availability of P impacts the rates of primary production, species distribution, and the very structure of an ecosystem (Benitez-Nelson, 2015; Paytan & McLaughlin, 2007; Ruttenberg, 2014)

1.3 Phosphorous Cycling

The global phosphorus cycle differentiates itself from other essential macro nutrients such as carbon (C) and nitrogen (N). While cycling through the earth system phosphorus maintains the same +5-oxidation state (PO_4^{3-}) throughout. This contrasts with

the C cycle where C can be found in a number of oxidation states such as CO_2 (+4), CO (+2), and CH_4 (-4) while N can be found in N_2 (+0), NO_2^- (+3), NO_3^- (+5) , and NH_4^+ (-3) to name a few (Erisman et al., 2013; Post et al., 1990). Another difference in the cycling of phosphorus is that atmospheric transport is for the most part unimportant, though dust transport and deposition can play an important role in some remote regions where other nutrient import flux low to non-existent, such as the Amazon basin (Barkley et al., 2019). This leaves the main components of the cycle as the sediment, terrestrial, and marine reservoirs. Just as the nitrogen and carbon cycles are being altered by humanity so too is the phosphorus cycle.

The sediment reservoir is the largest pool ($0.27 - 1.3 \times 10^{20}\ mol\ P$) and includes phosphorus contained in marine sediments, crustal rocks, and soils deeper than 60cm (Richey et al., 1993). The terrestrial phosphorus cycle can be further divided into two reservoirs: land, and land biota (Jahnke, R.A. 1992; Lerman et al., 1975). The land reservoir, soils less than 60cm deep (organic and inorganic P), contains $3100 - 6450 \times 10^{12}\ mol\ P$ (Richey et al., 1993). P stored in land biota accounts for $84 - 97 \times 10^{12}\ mol\ P$, despite being the smallest reservoir the interactions and fluxes between land biota and the other two reservoirs are crucial to the overall cycling of P as we will see (Richey et al., 1993).

For this discussion of the global P cycle we will start with plate tectonics. P contained in marine sedimentary minerals can be subducted or uplifted onto land depending on if the deposit is located on the continental margin or on a descending plate. Unlike C and N that are volatilized and released from the sediments as CO_2 and N_2 gas through volcanism and fossil fuel extraction and combustion, P has no important gaseous phase and is instead incorporated into crystalline apatite (Guidry & Mackenzie, 2000). Apatite ($Ca_{10}(PO_4)_6(OH, F, Cl)_2$) is the most common phosphate mineral, with fluorapatite being the most commonly mined for use in the production of fertilizer. The residence time of P incorporated in phosphorite deposits is on the order of $42 - 201 \times 10^6$yr, and is only introduced back to the terrestrial cycle through uplift and weathering (Richey et al., 1993). Weathering of apatite containing rock phosphate is accomplished mainly through interactions with acids, primarily produced from microbial activity, with a flux of $\sim 0.65 \times 10^{12} mol\ P\ \ yr^{-1}$ to the soil, with local rates influenced from temperature and surface area (Guidry & Mackenzie, 2000).

Phosphate is transported from the terrestrial environment to the marine in two ways, by rivers and by groundwater discharge (Maybeck, 1982). While being an important area of research over the past two decades the global groundwater discharge flux of P to the ocean is relatively unimportant (Moore, 2010). Although, at the regional scale groundwater P can play an important role in eutrophication leading to harmful algal blooms (Moore, 2010). In rivers ~95% of P is particulate due to phosphorus' particle reactivity, with an estimated flux of $0.59 - 0.65 \times 10^{12} mol\ P\ \ yr^{-1}$ (Meybeck, 1982; Ruttenberg, 2014). The chemical form that particulate P takes in the river is variable and can change in route to the ocean, it is influenced by geology, weathering rate, turbidity, and the river itself (Ruttenberg, 2014). A study by Berner and Rao (1994) determined that 20-40% of particulate P was organically derived. The dissolved P flux, $0.032 - 0.058 \times 10^{12} mol\ P\ \ yr^{-1}$, is split between the inorganic (DIP) and organic (DOP) forms (Meybeck, 1982). The partition between DOP and DIP is poorly constrained and does not appear to be connected to environmental factors (Ruttenberg, 2014).

Just as the chemical form of P in rivers is variable, P that enters the ocean is as well. Both particulate and dissolved P exhibit non-conservative behavior, both positive and negative, when entering the ocean (Fox, 1990). Dissolved P can be released from particulate P when entering high ionic strength marine waters as well as being diagenetically released from the sediment (Berner & Rao, 1994). Inversely, dissolved P can complex, flocculate, and settle out as particulate P and is further influenced by the rate of uptake from phytoplankton (R. A. Berner & Rao, 1994).

As demonstrated by Redfield (Redfield, 1958), the marine P cycle is intimately linked to photosynthetic fixation, export, and remineralization at depth. The result of being linked to photosynthetic activity is that it exhibits a typical dissolved nutrient profile with the surface water being depleted, a maximum near the O_2 minimum zone from remineralization (Atlantic: ~2.0μM, Pacific: ~3.0μM), and slightly decreasing (Atlantic: ~1.8μM, Pacific: ~2.6μM) towards the ocean floor (Sverdrup et al., 1942; Cavender-Bares et al., 2001). Phytoplankton uptake P in a relatively fixed ratio to the other macronutrients carbon and nitrogen of 106C:16N:1P (Redfield, 1958). Orthophosphate is directly consumed by primary producers, but in its absence, additional strategies are employed liberating tightly bound P in suspended sediment particles or organic molecules such as

metabolization of phosphonates by *Trichodesmium* (Paytan & McLaughlin, 2007). As such, the availability of P in the ocean impacts the rates of primary production, species distribution, and the structure of an ecosystem (Benitez-Nelson, 2015; Paytan & McLaughlin, 2007; Ruttenberg, 2014). Similar to land biota, oceanic biota exhibit efficient recycling of P, with a flux to/from the surface ocean of $19.5 - 35 \times 10^{12} mol\ P\ \ yr^{-1}$ (Mackenzie et al., 1993; Jahnke, 1992). The surface ocean is also supplied with P from upwelling of deep sea nutrient rich water with an estimated global flux of $1.87 \times 10^{12} mol\ P\ \ yr^{-1}$ (Lerman et al., 1975). P upwelling rates are dependent on the age of the deep water being upwelled with higher concentrations in the Pacific compared to the Atlantic (Jahnke, 1992). This is due to continuous primary production at the surface and export to depth along the global thermohaline circulation path (Lerman et al., 1975). The atmospheric deposition of P containing aerosols, volcanic ash, and dust is a very small pool and flux to the ocean overall, $0.02 - 0.05 \times 10^{12} mol\ P\ \ yr^{-1}$ (Jahnke, 1975). Yet, in open ocean atmospheric P deposition can be a vitally important input as ~30% the aerosolized P is soluble (Paytan & McLaughlin, 2007; Duce et al., 1991).

Settling, deposition, and burial of particulate P is the dominant sink in the ocean (Compton et al., 2000). Particulate rain from oceanic biota delivers $1.13 - 1.35 \times 10^{12} mol\ P\ \ yr^{-1}$ to the deep sea, with an additional $0.581 \times 10^{12} mol\ P\ \ yr^{-1}$ from downwelling in areas of deep water formation (Lerman et al., 1975; Mackenzie et al., 1993). The total flux of P from the ocean to the sediment is estimated at $0.265 - 0.280\ \times 10^{12} mol\ P\ \ yr^{-1}$, with an asymmetrical distribution favoring the continental margins where most P is delivered (Howarth et al., 1995; Ruttenberg, 1993). Thus, burial is dependent on location as well, with a burial flux from the sediments on the continental margin and the deep sea of $0.150 - 0.223 \times 10^{12} mol\ P\ \ yr^{-1}$ and $0.042 - 0.130 \times 10^{12}\ mol\ P\ \ yr^{-1}$ respectively (Howarth et al., 1995; Ruttenberg, 1993). An additional sink for P from the ocean was first discovered by Berner (1973) by iron-rich sediments in the East Pacific Rise, later attributed to sorptive removal in hydrothermal systems. Wheat et al. (2003) estimated this process produces a global flux of $0.036 \times 10^{12} mol\ P\ \ yr^{-1}$ back to the sediments.

A return flux of dissolved P from the sediment to the overlying waters occurs as a result of microbial respiration (Colman & Holland, 2000). In the sediment dissolved P is released during diagenesis and from iron-oxyhydroxides under reducing conditions (Crosby et al., 1984). The two processes release dissolved P into pore waters which can diffuse or be irrigated out of the sediment (Colman & Holland, 2000). The total P flux from the sediment back to the overlying waters is on the order of $0.51 - 0.84 \times 10^{12} mol\ P\ \ yr^{-1}$ and $0.41 \times 10^{12} mol\ P\ \ yr^{-1}$ for coastal and deep sea sediments respectively (Colman & Holland, 2000). In areas with a large supply of organic matter, diagenetic lithification can occur leading to phosphorite formation (Colman & Holland, 2000). Additional factors that influence phosphorite formation include warm temperature, high sea level, salinity, pH, and Ca/Mg ratio, as well as proximity to oxygen minimum zone boundaries (Burnett, 1977).

1.4 Anthropogenic Impacts on the Global P Cycle

Like most cycles, the P cycle is being significantly impacted by human activity, in particular for food production in the form of fertilizer, which accounts for 90% of phosphorus use in society (Cordell, 2010). Phosphorus is mainly obtained by the mining of phosphorite deposits, the phosphorus is separated from the rest of the matrix by beneficiation and is then treated with sulfuric acid to produce phosphoric acid (Cordell, 2010).

Since the 1850's fertilizer use has increased dramatically as a result of both food production growth and loss of topsoil from erosion, deforestation, and other farming and development practices (Dregne, 2002). From this shift in farming practices, perturbations to the dissolved P flux from land to the near shore have increased dramatically from $\sim 1.2 \times 10^{10} mol\ P\ yr^{-1}$ to $\sim 2.1 \times 10^{10} mol\ P\ yr^{-1}$ and is projected to rise by 25% by 2050 (Mackenzie et al., 2011; Mackenzie et al., 2002). The elevated P flux results in

eutrophication, harmful algal blooms, and hypoxic or anoxic conditions in aquatic environments across the globe (Caraco, 1995).

In Kaneohe Bay, Hawaii, riverine dissolved P demonstrates the anthropogenic effects of land use. During periods of increased storm-based runoff, sampling sites downstream of conservation sites and land under traditional agricultural practices experience little deviation from baseflow dissolved P levels (Hoover & Mackenzie, 2009). While, at sampling sites downstream of urbanized areas experienced strong positive perturbations in both P and N (Hoover & Mackenzie, 2009). Further, the increase in runoff has been linked to shifts in the limiting nutrient in the bay (Tanaka & Mackenzie, 2005). During periods of base flow Kaneohe bay is N-limited but following a large storm event a shift to P-limitation is observed from excess N in relation to P (Ringuet & Mackenzie, 2005). From these events an increase in phytoplankton biomass and gross primary productivity was observed in concert with a rapid decrease in nutrients (Ringuet & Mackenzie, 2005).

1.5 Determination of Phosphate in Natural Waters

Due to the importance of phosphorus as a nutrient and the increasing perturbations to the P cycle from human activity, P monitoring programs have expanded over the last century. Modern methods for P determination are based on the phosphomolybdenum blue (PMoB) reaction first described by Scheele in 1783 (Müller & Serain 2000). The general PMoB reaction proceeds in two steps. Step one involving the formation of a heteropoly polyoxometalate species around the phosphate anion, referred to as a Keggin ion first described by Keggin (1934). The second step involves the reduction of the Keggin ion to the deeply-blue 12-molybdophosphoric acid (MPA) product that is used for spectrophotometric detection (Nagul et al. 2015).

$$PO_4^{3-} + 12MoO_4^{2-} + 27H^+ \rightarrow H_3PO_4(MoO_3)_{12} + 12H_2O$$
$$H_3PMo(VI)_{12}O_{40} + Reductant \rightarrow [H_4PMo(VI)_8Mo(V)_4O_{40}]^{3-}$$

Since 1783, the PMoB method has undergone numerous improvements and iterations. All variations of the PMoB method share a commonality in that they require a strong acid, a source of Mo(VI), and a reductant (Nagul et al., 2015). Improvements in the PMoB method occur by variation of the acid and reductant employed and recommended concentration for each. Acids used in past methods include H_2SO_4, HCl, and $HClO_4$ (Fontaine, 1942; Harris & Popat, 1954; Sims, 1961; Ŗužička & Hansen, 1975). Reported reductants include: hydrazinium sulfate, hydroquinone, 1-amino-4-naphthol-2-sulfonic acid, ethanol, oxalyldihydrazide, 4-(methylamino)phenol sulfate, and ascorbic acid, among a multitude of others (El-Sayed et al., 2001; Hesse & Geller, 1968; Kriss et al., 1971; Sims, 1961).

Each combination of acid, reductant, and their concentrations combined with a P containing sample produce a broad absorbance spectrum, see Ch.2 and 4, across the visible-UV light spectrum (Nagul et al., 2015). From the absorbance spectrum, a maximum peak absorbance wavelength is determined and compared with a reference wavelength to determine the absolute absorbance (Ruzicka et al., 2019). The reference wavelength should be picked based on insensitivity to the analyte, in this manner the reference wavelength provides discrimination against reagent blanks and other complicating effects (Worsfold et al., 2013). The result being that the absolute absorbance is proportional to the concentration of P in the sample (Ruzicka et al., 2019). Each PMoB method, and in some cases the same one by a different author, reports a different maximum wave length for absorption (λ=680 to λ=900nm), molar extinction coefficient (ε=1000 to ε=32,500), and absorbance spectrum shape (Nagul et al., 2015; Ruzicka et al., 2019). This is significant, as there should be only a single value for each of these properties, which indicates that our understanding of the underlying chemistry is lacking (Ruzicka et al., 2019).

Perhaps the most notable improvement to the PMoB method came from Murphy and Riley (1962) who found that the presence of antimony (Sb (III)) accelerated the reduction of the Keggin ion to MPA by ascorbic acid and eliminated the need for heating the reaction. Using Sb(III) and ascorbic acid an Sb-PMoB species is formed with a twin peak absorbance spectrum at 880 and 710nm, the 880nm peak being slightly higher (Nagul et

al., 2015). The Murphy and Riley (1962) method provides the basis for most modern-day commercial P determinations.

1.6 Continuous Flow Analysis and Flow Injection

Traditionally, the PMoB method was accomplished by batch methodology, where there is a sequential addition of reagents to a fixed sample volume. The traditional paradigm changed with the invention of continuous flow analysis (CFA) by Skeggs, (1957). Skeggs (1957) showed that colorimetric analysis could be automated by using a multichannel peristaltic pump. The pump is used to continuously flow air-segmented samples through a long manifold, injecting reagents into each sample at confluence points in the manifold during flow (Skeggs, 1957). Segmenting samples with air-bubbles eliminated cross-over contamination between them. The confluence points in the manifold promote rapid mixing through turbulence, which is further enhanced by the pulsing nature of the peristaltic pumps (Skeggs, 1957). Using this method 100% mixing can be achieved such that batch assays can be easily adapted to CFA (Lundgren, 1960). To this effect, the PMoB method was quickly adapted to CFA as CFA improved sample throughput while maintaining sensitivity (Lundgren, 1960). Additionally, CFA eliminated the batch method need for temporal stability of the 12-molybdophosphoric acid (Lundgren 1960). Temporal stability is necessary for any batch method stemming from the sample preparation process, where multiple samples are prepared in advance followed by determination in sequence. With the time between preparation and determination for each sample being variable, as a result of its position in the sequence of preparation and determination. This required the reaction product to be stable for an extended period of time. By maintaining a consistent flowrate and manifold length for every assay, CFA standardized the reaction time, the time between when reagents are added to the reaction mixture and when the product is measured for P absorbance (Lundgren 1960).

To prevent the formation of residue in the manifold and maintain air bubble consistency in CFA a surfactant was added to the reagent mixture. Discussion of the analytical consequences regarding the type and amount of surfactant were neglected until a recent study conducted by Hatta et al. (2019). Hatta et al. (2019) found that different surfactants could change the absorbance spectrum of the Sb-PMoB, increase the sensitivity of the reaction, and increase the reaction speed.

Sample throughput was further improved with the invention of Flow Injection Analysis (FIA) which eliminated the need for air-segmentation, allowing the PMoB method to be adapted to FIA (Ruzicka and Hansen, 1975; Ruzicka & Stewart 1975).

While providing huge improvements over batch methods, CFA and FIA are not without their drawbacks. In order to accommodate the high throughput, continuous flow methods employ a short measurement period, i.e., the time in which an individual reaction mixture is directly in the detector. This means that determinations can only be made as the reaction mixture passes through the detector. This precludes kinetic analysis of the reaction as it progresses. Another drawback of continuous flow methods is that they require a length of tubing and manifold that is appropriate for the reaction time needed. The longer the length of tubing the larger the surface area, which presents an issue for temperature control and requires continuous cleaning and replacement. Finally, continuous flow methods use larger volumes of reagents and sample as reagents flow continuously. The large manifold and quantity of reagents used in CFA and FIA prohibit further miniaturization and thus make them unfeasible for in-situ applications. Notwithstanding, all flow-based assay are performed using CFA, with sample collection accomplished manually by individuals.

1.7 Principals of µSIA

First developed by Ruzicka and Marshal (1990), micro sequential injection analysis (µSIA) represents the second generation of flow injection analysis techniques and solved

many of the problems inherent to CFA and FIA. μSIA uses precisely controlled discontinuous bi-directional flow accomplished by means of a pump in conjunction with a miniaturized multi-channel Lab-on Valve (LoV, Figure 1). Flowrates and aspirated/transferred volumes are achieved by computer control of the pump and LoV. This method of control, coupled with the precision of the pump, provides a high degree of reproducibility and precision, typically < 2%. The μSIA technique only requires μL volumes of sample and reagent to accomplish the reaction and analyte detection, whereas CFA requires mL volumes. The relatively small reagent and sample volumes enabled the μSIA manifold to be miniaturized (Figure 2). It is the miniaturization, encapsulation, and deployment of the μSIA manifold and PMoB method that is the subject of this work.

In μSIA a pump aspirates sample and reagents in sequence from each port on the LoV into a holding coil filled with carrier solution (typically deionized water). The direction of flow is then reversed and the reaction mixture is dispensed into a flow cell for spectrophotometric detection (Figure 1, Figure 2). Reaction product detection can be accomplished through one of two protocols. The first method is to stop the reaction mixture in the flow cell. This stopped in flow cell (SFC) technique is achieved by proceeding all the way from A-C in Figure 3. SFC permits direct observation of the kinetics of the reaction within the flow cell as the reaction proceeds, an impossibility in traditional flow systems. The second method of detection in μSIA is to stop the reaction mixture in the holding coil. The stopped in holding coil method (SHC) is achieved by holding the sample in the holding coil (Figure 3-B) while the reaction proceeds. After a set reaction time has elapsed the reaction mixture is aspirated continuously through the flow cell. The SHC method is similar to a conventional flow system where the final reaction product is detected as it passes through the flow cell.

In this work the SFC method is the method employed allowing us to observe the kinetics of the PMoB reaction and optimize the reaction chemistry. During development the SHC protocol was also employed in determining the volumes to dispense and mixing for the SFC protocol.

1.8 Mixing in a µSIA Regime

While µSIA represents an improvement of flow injection analysis techniques it does introduce a few new problems. The biggest problem in a single pump µSIA system is found in the incomplete mixing between reagents and samples in the holding coil. The issue arises as a result of the sequential nature of the reagent injections into the small-bore tubing which results in mixing between reagents only occurring at the interfaces. In cylindrical tubing, laminar flow results in a parabolic profile as fluid at the tubing wall flows more slowly, due to friction, than fluid near the center of the tube (Figure 4). Mixing at the interface between reagents during laminar flow is fairly limited. If in the flow cell, the interface between two segments creates a refractive index effect which leads to poor reproducibility from light distortions, this is especially pronounced with major refractive index differences. Further, poor mixing between reagents can produce unwanted by-products. In particular for PMoB methods, sub-optimal reagent concentrations can produce a blue residue that binds to the inside of the tubing. During operation particles from residue can be resuspended and lead to reproducibility issues when they interfere with light in the detector.

In contrast to µSIA, CFA and FIA achieve good mixing as a result of continuous flow past the confluence points resulting in reagents and sample mixing within the manifold. In a single pump µSIA confluence points are not possible. In order to obtain the best detection limit for the analyte, the sample and reagents must mix completely over a very short distance to achieve the optimum reaction conditions.

To get around the problem of mixing, turbulent radial mixing can be induced in µSIA by discontinuous bi-directional flow, such as flow direction reversals, acceleration, abrupt stops, bursts of high flow velocities, as well as changes in the geometry of the manifold itself, all of which are employed in the method presented in this work. Note that the newest generation of FIA techniques, programable Flow Injection (pFI), solves the one pump µSIA mixing problem. pFI accomplishes this with the addition of a second pump and confluence points directly inside the pFI manifold (Ruzicka, 2016).

While progress has been made on ramping up nutrient monitoring programs across the world in an attempt to better understand the effects anthropogenic activities have had on global cycles and the environment, much work is still needed. Progress in this area is mainly limited by our ability to make measurements at relevant spatial and temporal scales. This limitation is not due to our ability to process samples but our ability to collect them as it requires manual collection and sample preservation. Due to the magnitude of the P perturbations from anthropogenic practices, an autonomous automated system with P determination sensitivity an order of magnitude worse than current CFA, FIA, or μSIA methods would still provide researchers with invaluable insight. This work is meant to provide the groundwork for a μSIA, multi-assay, in-situ, nutrient auto analyzer using P as a proof of concept.

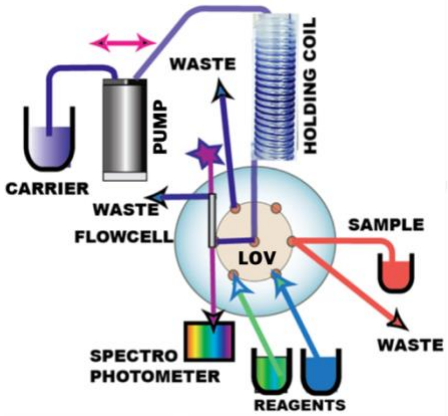

Figure 1: Depiction of a µSIA system

Cartoon depiction of an µSIA system, including a pump used for bi-directional flow, a holding coil connected to the pump and LoV used as a reaction vessel for reagent mixing, LoV providing multi-channel selection of reagents for flow programing, spectrometer for detection of reagents in the flow cell, and a flow cell that provides a straight path for which light can be directed through to the spectrophotometer (flowinjectiontutorial.com).

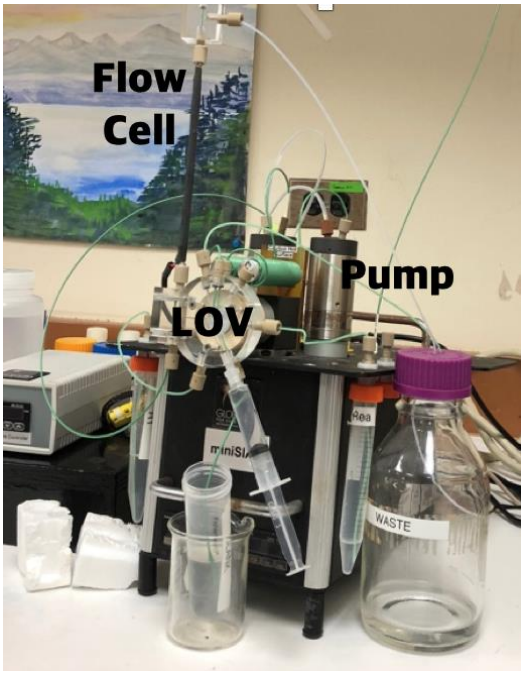

Figure 2: Commercially produced µSIA platform

Commercially produced µSIA platform (miniSIA) produced by GlobalFIA. The miniSIA system is designed to accommodate both µSIA and pFI through the inclusion of two pumps and holding coils.

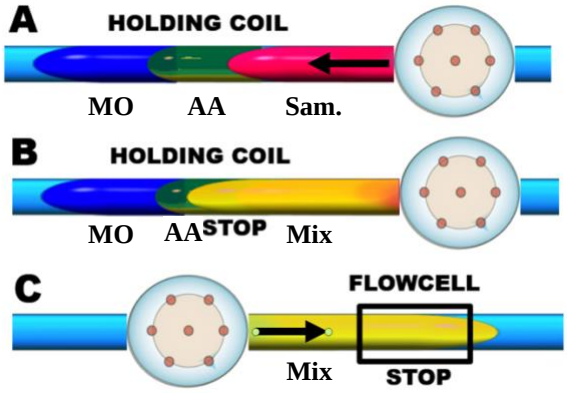

Figure 3: µSIA flow protocol

Depiction of the µSIA flow protocol using PMoB reactants, MO is mixed molybdate, AA is ascorbic acid, Sam. is the sample, and Mix is the reaction mixture (descriptions of the reactants found in Ch.2). (A) Sequential injection of reagents into holding coil common to all µSIA methods, reagents are aspirated in sequence through the LoV into the holding coil. (B) Stop in holding coil (SHC), reagents are stopped in the holding coil and allowed to mix for a given period of time. (C) Stop in flow cell (SFC), in addition to or instead of SHC reagents are dispensed from the holding coil through the LoV to the flow cell and stopped allowing the reaction to be observed by spectrophotometric detection. (flowinjectiontutorial.com)

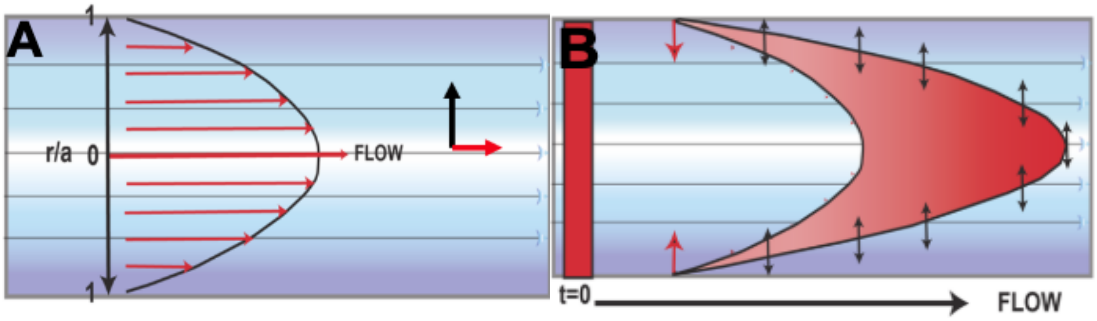

Figure 4: Physics of laminar flow in cylindrical tubing

Cartoon depictions of laminar flow in cylindrical tubing, (A) depicts the formation of a parabolic profile through the reduction of velocity (red arrow) by drag created by proximity to the tubing walls. (B) depicts radial mixing between two reagents along the surface area of a parabolic flow profile, radial mixing is also influenced by density differences between the two reagents. (flowinjectiontutorial.com)

Chapter 2. Chemistry

In adapting the PMoB method for use on an autonomous μSIA in-situ auto analyzer a number of problems were encountered. First, the nature of sequentially adding reagents into a small-bore tubing (0.75mm diameter) introduces uncertainty regarding mixing leading to residue deposition in the manifold and refractive index issues. Second, any autonomous reagent-based auto analyzer requires all volumes of reagent, carrier, and waste be stored on board. Minimizing reagent use therefore has a direct impact on the duration an auto analysis system can be deployed. Finally, typical dissolved PO_4 concentrations in Hawaii's near shore environment fall in the ~0-3μM PO_4 range, the analytical method must measure in this range with the lower the detection limit the better (Hoover & Mackenzie, 2009). In this chapter we will describe the results of the method development.

2.1 Experimental Conditions

All experiments were undertaken in the lab at 20°C using distilled water based PO_4 standards. A full description of the μSIA manifold can be found in Ch. 3.1. A flow cell of 142mm length, internal diameter 0.75mm (volume = 62.7μL) was used for all experiments. The SFC protocol was used for all experiments using the sequence described in Ch. 3.4 for aspirating reagents and sample into the holding coil. The total volume dispensed from the holding coil to the flow cell was 155μL (except where noted). The incubation time of the reacting mixture in the flow cell was varied for each method and is noted in the following section.

The final absorbance of the PMoB product was determined using a 710nm wavelength (except where noted) and 515nm as a reference using the following equation:

$$\text{Final Abs.} = (\text{Abs}[710] - \text{Abs}[515])_{end} - (\text{Abs}[710] - \text{Abs}[515])_{bs}$$

Where $(\text{Abs}[710] - \text{Abs}[515])_{end}$ is the average of the absorbance values collected during the last 5 seconds of the reaction monitoring period, and $(\text{Abs}[710] - \text{Abs}[515])_{bs}$ is the baseline absorbance. Baseline absorbance values were obtained by spectrophotometric measurement of each sample or standard without the addition of the reagents. The duration of the reaction time is method specific and is described below. The limits of detection (LOD) were calculated as 3 times the standard deviation of the concentration of the lowest standard. Where appropriate, standard deviations are reported and are normalized to N-1.

2.2 List of Reagents for PMoB Method

Deionized (DI) water was generated by a Barnstead water purification system, Nanopure Diamond (18.2 mΩ; Thermo Fisher Scientific, www.thermofisher.com).

Potassium antimony(III) oxide tartrate trihydrate ($C_8H_4K_2O_{12}Sb_2{\cdot}3H_2O$; Sigma-Aldrich, https://www.sigmaaldrich.com). A stock solution (KSb) was produced using 0.45g potassium antimony(III) oxide tartrate trihydrate dissolved in 45mL of DI water. Solution was stored refrigerated.

Ammonium molybdate tetrahydrate, (AMo; $(NH_4)_6Mo_7O_{24}{\cdot}4H_2O$; certified ACS; Fisher Scientific, https://www.fishersci.com)

Sulfuric acid (H_2SO_4; 36N; certified ACS. Fisher Scientific, https://www.fishersci.com)

Hydrochloric acid (HCl; Certified ACS plus; Fisher Scientific, www.fishersci.com) purified by sub-boiling distillation to 6.54N.

Ascorbic acid ($C_6H_8O_6$; Alfa Aesar, https://www.alfa.com/)

Brij 35 a nonionic surfactant, (polyethylene glycol dodecyl ether; Sigma-Aldrich, https://www.sigmaaldrich.com)

Sodium dodecyl sulfate an anionic surfactant (SDS; $CH_3(CH_2)_{11}SO_4Na$; Affymetrix; Thermo Fisher Scientific, www. thermofisher.com)

Phosphate standard solution (1000ppm; LabChem, https://www.labchem.com/). A 50µM PO_4 working standard was produced by serial dilution with DI acidified to 0.025N with HCl.

Low nutrient surface sea water samples (LNSW) were collected by Morgan Linney of the Hawaii Ocean Time-series program at station ALOHA, in the North Pacific Ocean. LNSW is filtered through a 0.45µm filter (Supor 450 Membrane filter, Pall, https://shop.pall.com/, expected PO_4 concentration of < 10nM)

2.3 Individual Method Reagents

The PMoB method uses two reagents, mixed molybdate reagent (MO) and an ascorbic acid reductant (AA), the variations of which are the basis of the different methods. The following sections describe the make-up of each reagent assay employed in this work. In addition, the reagent assays are described in Table 1.

2.3.1 One-Pump Method (H_2SO_4-No-Surfactant), Hatta et al.(2018)

MO: 4mL of the KSb stock solution, 0.35g of AMo, 8mL of H_2SO_4, made up to 200mL with DI

AA: DI with a 3% ascorbic acid (w/v concentration)

Carrier: DI

2.3.2 One-Pump Method Using Sulfuric Acid and Brij (H_2SO_4-Brij)

MO: 4mL of the KSb stock solution, 0.35g of AMo, 4mL of H_2SO_4, made up to 200mL with DI

AA: DI with a 3% ascorbic acid (w/v) and 0.5% Brij concentration

Carrier: DI

2.3.3 One-Pump Method Using Sulfuric Acid and SDS (H_2SO_4-SDS)

MO: 4mL of the KSb stock solution, 0.35g of AMo, 4mL of H_2SO_4, made up to 200mL with DI

AA: DI with a 3% ascorbic acid (w/v) and 6% SDS concentration

Carrier: DI

2.3.4 One-Pump Method Using Hydrochloric Acid and SDS (HCl-SDS)

MO: 1.2mL of the KSb stock solution, 0.75g of AMo, 36.7mL of 6.54N HCl, made up to 200mL

AA: DI with a 2.2% ascorbic acid (v/w) and 1.3% SDS

Carrier: DI with a 0.1% SDS (v/w) concentration

2.4 Surfactant Influence

The initial plan for the field deployable µSIA-PO_4 auto analyzer was to directly adopt the one pump µSIA-PO_4 no-surfactant method (reagents described in section 2.3.1) developed by Hatta et al. (2018). This method was simple to directly implement on the µSIA system as it was developed for µSIA applications. We confirmed the results found by Hatta et al. (2018), in that the method produces reliable non-linear calibration curves (Figure 5).

Fluctuating temperatures in the natural environment require frequent calibration. In a laboratory environment access to mains electricity allows for the use of energy intensive thermostatted flow cells and holding coils. These components significantly enhance reaction rates and standardize reaction temperatures. Controlling reaction temperature means that calibration curves need only be produced periodically as needed. The power limitations of in-situ operations prevented the use thermostatted components leading to environmentally determined reaction temperatures. Fluctuating reaction temperatures require a calibration curve be produced for each analytical cycle.

Due to the need to produce a standard curve for each analytical cycle the non-linear nature of the calibration curves produced by the Hatta et al. (2018) method made it less practical for in-situ applications since a non-linear standard curve requires a minimum of

five standards to analyze a sample, whereas a linear calibration curve requires three. The two additional standards required for non-linear curves consume ~20% more power, reagent, and carrier while producing more waste than a linear curve, thereby limiting deployment times. Further, the extra standards, reagent, carrier, and waste volumes add to the total package volume. Altogether, the additional power and volume requirements imposed by a non-linear calibration curve prompted the investigation of the influence of surfactants (Brij-35 and sodium dodecyl sulfate) in a single-pump µSIA system. Investigating the use of surfactants on calibration curve linearity in a µSIA system was spurred by work published by Hatta et al. (2019). Hatta et al. (2019) demonstrate the influence of surfactant use on method sensitivity in a pFI system, and as a result produced linear calibration curves and an improved reaction speed when compared to CFA. Hatta et al. (2019) posit that PMoB is colloidal in the acidic environment of the reaction, but when exposed to a surfactant is stabilized inside the resulting micelles by the non-polar tails.

2.4.1 Effect of the Brij 35 Surfactant

Figure 6 compares the absorbance spectrums produced using both the Hatta et al. (2018) and the H_2SO_4-Brij methods (reagents described in 2.3.2). The general structure of the two spectra are similar in that they both produce dual absorbance peaks at 715nm and 880nm (Figure 6). Note that while the 880nm peak is the more pronounced of the two, it is outside of the effective working range of the spectrometer employed in this project. The largest difference between the two one-pump methods is that absorbance using Brij was enhanced 4-fold over that of the non-surfactant Hatta et al. (2018) method. Further note that the H_2SO_4-Brij spectrum was obtained after 600sec while the non-surfactant spectrum was obtained after 120sec, though as shown in Figure 6 the H_2SO_4-Brij absorbance exceeds that of the non-surfactant after ~30sec.

Figure 7 shows the reaction progress of the H_2SO_4-Brij method in the flow cell as it proceeds over a 600sec period. The reaction curve is characterized by three distinct phases, the timing of which is dependent on PO_4 concentration. The first phase of the

reaction proceeds quickly with a steep increase in absorbance (Figure 7-Box 1). The second phase shows that the reaction reaches an absorbance maximum followed by decline (Figure 7-Box 2). The final phase sees the absorbance decline of the second phase level off, eventually reaching a plateau (Figure 7-Box 3).

The ability to directly observe the reaction allowed for an investigation of the phase two decline. Through the use of analytical software developed for this project that allowed the observation of raw data in new formats that were not possible with commercially available software, it was discovered that the absorbance spectrum for H_2SO_4-Brij method shifted during the 600 second reaction time. Following a peak in absorbance at 760nm at ~300sec the absorbance spectrum shifts from the single peak spectrum during phase two to the dual peak spectrum of 710nm and 880nm (Figure 8).

Despite the changing absorbance spectrum, a linear calibration curve can be produced using 710 and 515nm wavelengths after a reaction time of 600sec. The limit of detection for the H_2SO_4-Brij method, under the laboratory conditions, was 39nM PO_4 (Figure 9). The calibration curve is not linear until the end of phase 3 due to the shift in the absorbance spectrum from the single peak to the double peak.

As for why the shift in the absorbance spectrum occurs a combination of both physical and chemical effects provides possible explanations. As Hatta et al. (2019) posits, the blue tint of the reaction product and broad absorbance spectrum indicate that the physical Tyndall effect of nanoparticle light scattering may be occurring from colloidal aggregation of PMoB into particles. This is evidenced by observed blue residue deposited on the interior of the manifold tubing. Evidence for the chemical nature of the shift comes from the magnitude of the decline observed in phase 2 between the 1.5 and 3.0µM PO_4 standards. The magnitude of the decline is a result of a decline in absorbance at the 710nm, collapse of the 760nm peak, and an increase in absorbance at the 515nm and the lower wavelength range as a whole. While the increase in the reference wavelengths indicates a general scattering of light, the collapse of the 760nm peak indicates that what is occurring is a new product being formed. As the reaction proceeds from phase 2 to phase 3, and the absorbance plateaus, an equilibrium between the two products is formed. This is indicated by the convergence of the calibration curve towards linearity, as the higher concentration

standard continues to decline after the lower standard has plateaued (Figure 7). Whatever the cause, the observed absorbance spectra shift from the single to the double peak spectra offers clues into the inner machinations of the PMoB chemistry.

2.4.2 Effect of the Sodium Dodecyl Sulfate Surfactant

The complicated nature of the absorbance shift and long reaction time of the H_2SO_4-Brij method prompted an exploration of other surfactants for inclusion in the PMoB assay. Sodium dodecyl sulfate (SDS) presented the most logical choice for testing due to its widespread inclusion in CFA PMoB assays. Further, as SDS's use in CFA is mainly for the prevention of residue formation in the manifold, it served the dual function of cleaning the system as well (Nagul et al., 2013).

The H_2SO_4-SDS method produces a dual peak absorbance spectrum with absorbance peaks at 710nm and 880nm (Figure 10). The inclusion of SDS in the reaction increases absorbance ~3.5x over that of the Hatta et al. (2018) method (Figure 10). Figure 11 shows the reaction curves for the H_2SO_4-SDS method. The reaction simply increases in absorbance with time reaching a plateau at ~400sec. Using absorbances 710nm for the reaction product wavelength with a 515nm reference wavelength after a 410sec reaction time, the H_2SO_4-SDS method produces a linear calibration curve (Figure 12). The slope of the H_2SO_4-SDS method calibration curve is ~20% lower than that of the H_2SO_4-Brij method, H_2SO_4-Brij = 0.098AU/µM and H_2SO_4-SDS = 0.080AU/µM (Figure 9, Figure 12).

Both Brij and SDS increase absorbance of the reaction product. The differences in the magnitude of the effect over the Hatta et al. (2019) method and the progression of the reaction are most likely a result of the ionic nature of the surfactants. Brij is a nonionic surfactant that forms long chains while SDS is anionic and forms micelles that stabilize the reaction product (Hatta et al., 2019). As for how and why the Brij eventually produces a single peak spectrum then evolving to the two peak spectrum, while SDS only produces the two peak spectrum is beyond the scope of this thesis.

2.5 Effect of HCl as a Source of Protons

Using a two-pump pFI technique Ruzicka et al. (2019) further optimized the PMoB method describing optimal reaction concentrations in the flow cell of [Mo] = 1.0 mM, [H^+] = 0.4 N, KSb = 0.03mM, ascorbic acid = 0.75%, and SDS = 0.38%. Ruzicka et al. (2019) suggests the use of HCl over H_2SO_4 to supply the protons, as monoprotic acids disassociate completely. The absorbance spectrum produced using HCl for the source of protons, with SDS and the initial concentrations described in section 2.3.4, has a similar shape to that of the H_2SO_4-SDS (Figure 13). While the general shape of the spectrums is similar Figure 14 shows the difference in the reaction curves, with HCl-SDS being much faster to react.

The one-pump HCl-SDS method's reaction curve is characterized by two distinct phases with a transition between them. In the first phase (~50sec) the reaction proceeds quickly producing a steep non-linear initial increase in absorbance (Figure 15). The initial phase is followed by a transition period (~50-75sec) in which the increase in absorbance is still non-linear but provides results similar to the second phase as we will show. The second phase (~75) is characterized by a linear increase in absorbance with time (Figure 15).

The linearity of the absorbance increase in phase 2 of the reaction allows a calibration curve to be produced from the slope of the reaction curve (Figure 16). Figure 16 shows that the slopes produced during phase 2 by each standard from the 175-195sec time points are linearly corelated. Therefore, the length of time the reaction is allowed to proceed directly corelates with the slope of the calibration curve. As such, a calibration curve can be produced at any time point after phase 1, even during the non-linear transition phase, for DI based standards ~50sec (Figure 17). Table 2 and Figure 17 show the slopes and limits of detection at various times during the transition and second phase of the reaction. Altogether, the choice of using HCl over H_2SO_4 results in a +50% increase in calibration curve slope (slope = 0.08AU/µM for H_2SO_4 and slope = 0.126AU/µM for HCl) in only 250s vs 410s (Figure 17-C). The results from Figure 17 A-C are interesting, as time progresses both the LOD and R^2 increase. The observed R^2 increase is a result of the full

transition to phase 2. During the transition phase (Figure 17-A, 50sec) the increase in absorbance is still non-linear, with the rate of absorbance increase being slightly different between the two PO_4 spiked standards, though the R^2 still indicates high correlation. Following the start of the second phase (Figure 17-B and C, 75 and 250sec respectively), with linearly increasing absorbance, the rates between the different standards converge. The increase in the LOD between Figure 17 A and C may indicate that a secondary product is forming, but this is unlikely. As the LOD is calculated from 3x the standard deviation of the lowest standard a slight increase in the standard deviation of the blank between 50 and 250sec accounts for this, even so a 19nM PO_4 LOD is among the lowest reported for comparable methods.

2.6 Intercomparison study

An intercomparison study was performed by Dr. Hatta to confirm the results of the one pump HCl-SDS method. The study was performed using the miniSIA pFI platform (two-pump system, GlobalFIA) using a spectrometer capable of measuring the 880nm wavelength peak. Dr. Hatta was only provided with the reagent concentrations list (Ch. 2.3.4 and Table 1). In the study the HCl-SDS method presented in this work was compared against the two pump pFI assay described above in Ch. 2.5 and published by Ruzicka et al. (2019). Both methods were used to measure a set of PO_4 spiked DI standards. From the PO_4 standards calibration curves (n=3) were produced using 550nm as the reference wavelength and both 880nm (Figure 18) and 700nm (Figure 19) as the reaction product wavelength. The results of the intercomparison confirm results presented above with the HCl-SDS µSIA-PO_4 method performing ~10% more sensitively than the Ruzicka et al. (2019) method for the 880nm peak (slope = 0.1561AU/µM vs. slope = 0.1409AU/µM) and ~46% more sensitive for the smaller 700nm peak (slope = 0.1069AU/µM vs. slope = 0.0726AU/µM).

Table 1: Method Reagents

One-Pump Assays	MO	AA (w/v) in DI	Carrier
H_2SO_4-No-Surfactant (Hatta et al., 2018)	KSb: 4mL AMo: 0.35g H_2SO_4: 8mL DI: Up to 200mL	Ascorbic acid: 3%	DI
H_2SO_4-Brij (this work)	KSb: 4mL AMo: 0.35g H_2SO_4: 4mL DI: Up to 200mL	Ascorbic acid: 3% Surfactant: Brij 35, 0.5%	DI
H_2SO_4-SDS (this work)	KSb: 4mL AMo: 0.35g H_2SO_4: 4mL DI: Up to 200mL	Ascorbic acid: 3% Surfactant: SDS, 6%	DI
HCl-SDS (this work)	KSb: 1.2mL AMo: 0.75g HCl: 36.7mL DI: Up to 200mL	Ascorbic acid: 2.2% Surfactant: SDS, 1.3%	DI with 0.1% SDS (w/v)

Table 2: One-pump HCl-SDS method reaction time comparison

Reaction Window:	**50s**	**75s**	**250s**
Slope	0.090	0.096	0.126
Limit of Detection:	14nM	18nM	19nM

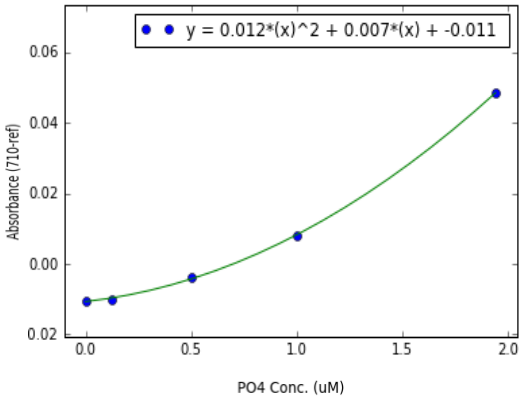

Figure 5: H_2SO_4-No-Surfactant calibration curve

Non-linear calibration curve produced using the one-pump µSIA H_2SO_4-No-Surfactant (see text in section 2.4.2). Obtained using PO_4 (µM) spiked DI standards after a 120sec reaction time with reaction and reference wavelengths of 710nm and 510nm respectively.

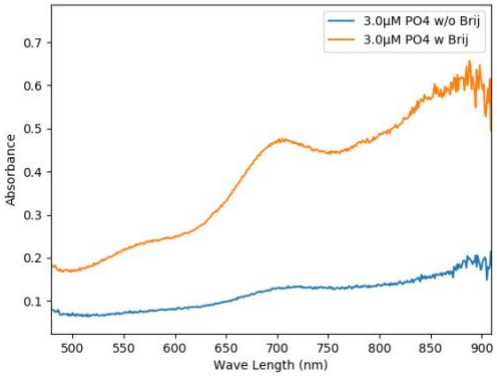

Figure 6: Absorbance spectrum comparison obtained using the one-pump H_2SO_4-Brij and the one-pump H_2SO_4-No-Surfactant methods

Absorbance spectrums of a 3.0µM PO_4 spiked DI standard acquired after a 600sec reaction using the H_2SO_4-Brij (orange) and 120sec using the H_2SO_4-No-Surfactant Hatta et al. (2018) method (Blue). Absorbance is calculated by taking a reference measurement to an unreacted aliquot of the 3.0µM PO_4 spiked DI standard.

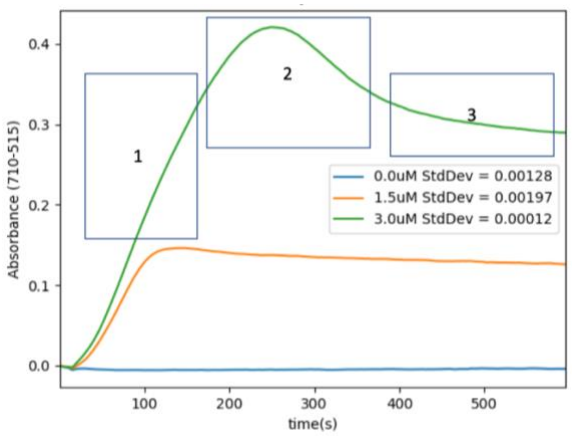

Figure 7: H_2SO_4-Brij reaction curves

Evolution of the reaction curves (n=3 for each curve, standard deviations for final absorbance values) for the H_2SO_4-Brij method for three different PO_4 (µM) spiked DI standards. Absorbances acquired using a 515nm reference wavelength and 710nm reaction wavelength over a 600sec reaction time. Boxes 1-3 show the distinct phases that characterize the H_2SO_4-Brij reaction curve.

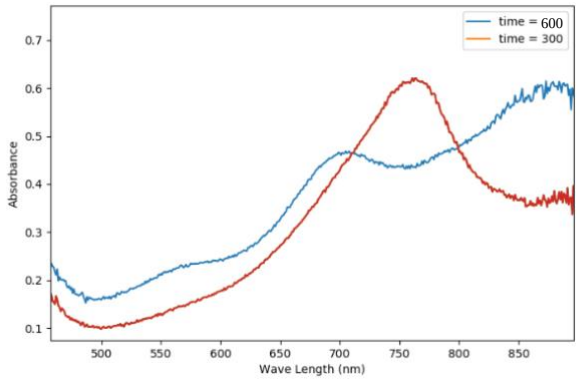

Figure 8: H_2SO_4-Brij method absorbance spectrum evolution

H_2SO_4-Brij method absorbance spectrums for a 3.0µM PO_4 spiked DI standard after 300sec (red) and 600sec (blue). Absorbance is calculated by taking a reference measurement to an unreacted aliquot of the 3.0µM PO_4 spiked DI standard.

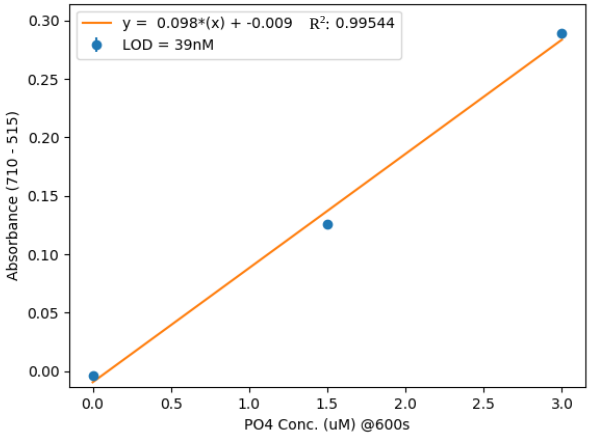

Figure 9: H_2SO_4-Brij method calibration curve

Calibration curve for PO_4 (µM) spiked DI standards (n=3 for each data point, error bars shown but smaller than data points) obtained using the H_2SO_4-Brij method. Absorbance values were obtained using 710nm reaction wavelength and a 515nm reference wavelength after 600sec reaction. The LOD obtained was 39nM PO_4 with an R^2 of 0.9954.

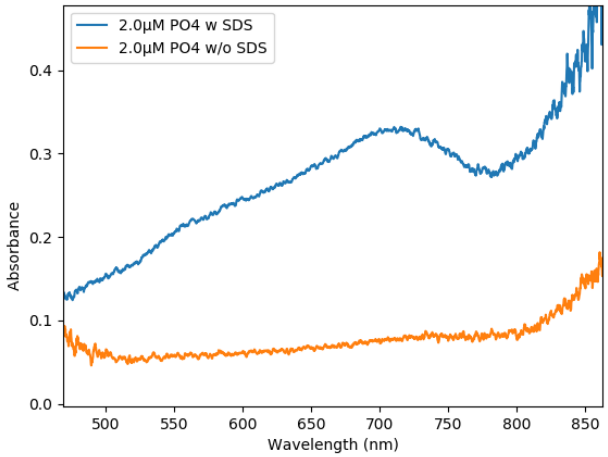

Figure 10: Absorbance spectrum comparison of H_2SO_4-SDS and H_2SO_4-No-Surfactant

2.0µM PO_4 spiked standard absorbance spectrums acquired after 400sec reaction using the one-pump H_2SO_4-SDS method (blue) and 120sec using the one pump H_2SO_4-No-Surfactant Hatta et al. (2018) method (orange). Absorbance is calculated by taking a reference measurement to an unreacted aliquot of the 2.0µM PO_4 spiked DI standard.

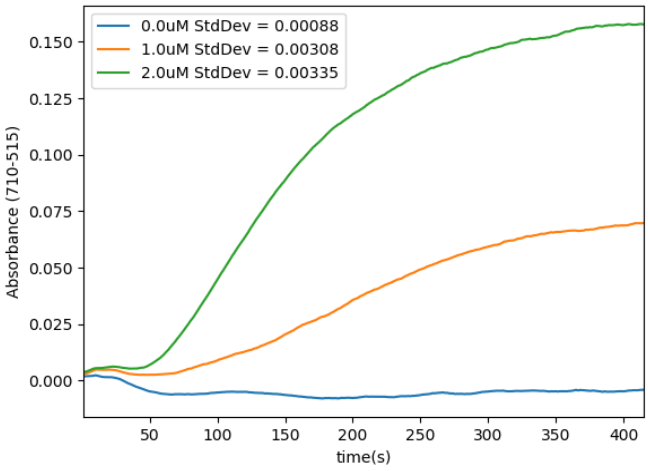

Figure 11: H_2SO_4-SDS reaction curves

Reaction progress curves (n=3 for each curve, standard deviations for final absorbance values) for the one-pump H_2SO_4-SDS method for different PO_4 (µM) spiked DI standards. Acquired using 710nm for the reaction wavelength with a 515nm reference wavelength with a 410sec reaction time.

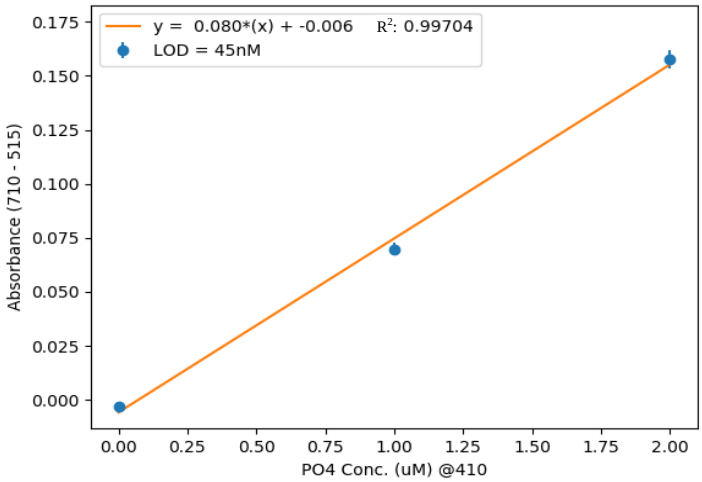

Figure 12: H_2SO_4-SDS method calibration curve

Calibration curve of different PO_4 (µM) spiked DI standards (n=3 for each data point) obtained using the H_2SO_4-SDS method. Absorbance values obtained using 710nm for the reaction wavelength with a 515nm reference wavelength and after 410sec reaction window. The LOD obtained for the method is 45nM PO_4 with an R^2 of 0.997.

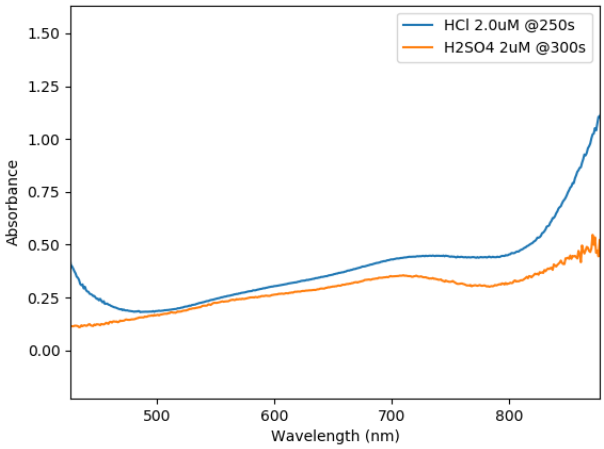

Figure 13: Absorbance spectrum comparison between the one pump H_2SO_4-SDS and one pump HCl-SDS methods

2.0µM PO_4 spiked DI standard absorbance spectrum comparison between H_2SO_4-SDS (at 300s, blue) and HCl-SDS (at 250s, orange). Absorbance is calculated by taking a reference measurement of an unreacted aliquot of the 2.0µM PO_4 spiked DI standard.

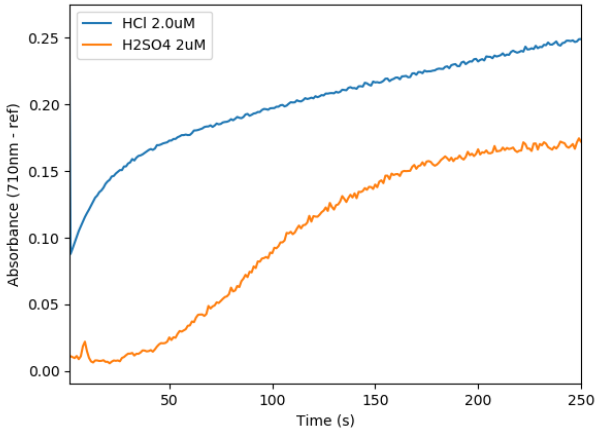

Figure 14: Reaction curve comparison between the one-pump H_2SO_4-SDS and the one-pump HCl-SDS methods

Change in absorbance as a function of time during the reaction of a 2.0µM PO_4 spiked DI standard using both the H_2SO_4-SDS (orange) and HCl-SDS (blue) methods. Absorbance values obtained using 710nm for the reaction wavelength with a 515nm reference wavelength.

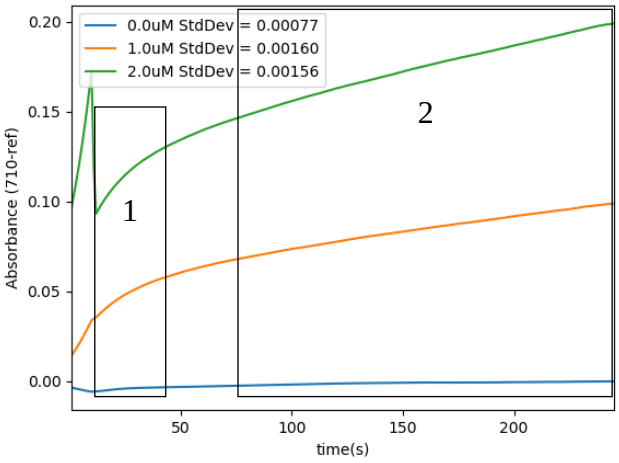

Figure 15: HCl-SDS reaction curves

HCl-SDS averaged reaction curves (n =3 for each curve, standard deviations for final absorbance values) for different concentration PO_4 (µM) spiked DI standards, acquired using a 710nm for the reaction wavelength with a 515nm reference wavelength over a 250sec reaction time. Boxes 1 and 2 show the distinct phases that characterize the HCL-SDS reaction curves.

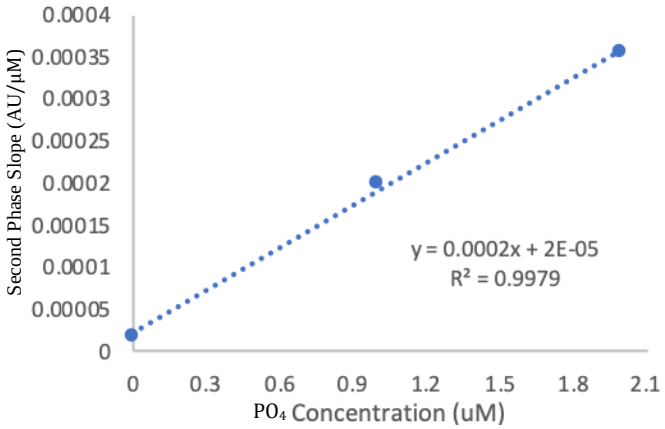

Figure 16: HCl-SDS 2nd phase slope calibration curve

Slopes produced by PO_4 (µM) spiked DI standards during the 2nd phase from 175-195sec of the reaction curve using the HCl-SDS method. Absorbance values from the reaction curves obtained using 710nm for the reaction wavelength with a 515nm reference wavelength.

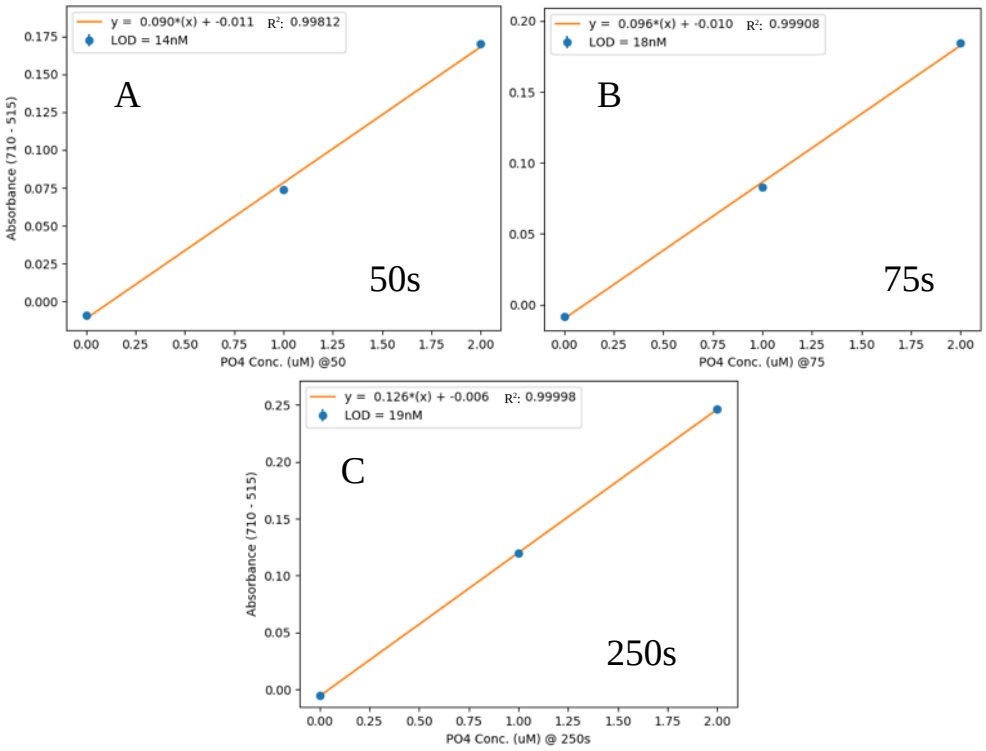

Figure 17: Time evolution of the one pump HCl-SDS method calibration curves

HCl-SDS calibration curves using PO_4 (µM) spiked DI standards (n=3 for each point, error bars shown but smaller than symbol) produced at (A) 50sec (LOD=14nM, R^2=0.9981), (B) 75sec (LOD=18nM, R^2=0.9991), and (C) 250sec (LOD=19nM, R^2=0.9999), acquired using 710nm for the reaction wavelength with a 515nm reference wavelength.

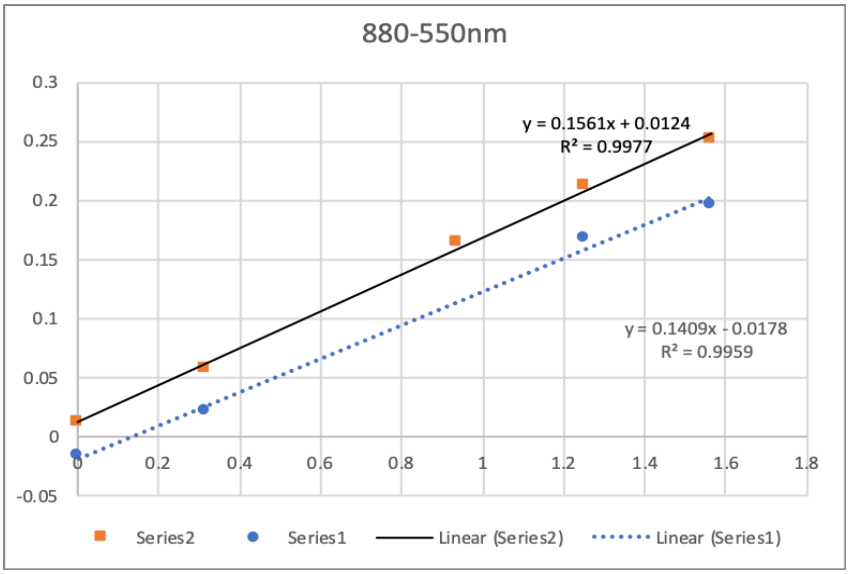

Figure 18: HCl-SDS method one-pump method vs Ruzicka et al. (2019) two pump pFI intercomparison study

Calibration curves from the intercomparison study using 880nm wavelength with a 550nm reference wavelength. (Series-1) Ruzicka et al. (2019) pFI method (blue), R^2=0.9959. (Series-2) HCl-SDS µSIA method (orange, this work), R^2=0.9977. Y-axis is absorbance of 880-550nm, X-axis is p concentration in µM.

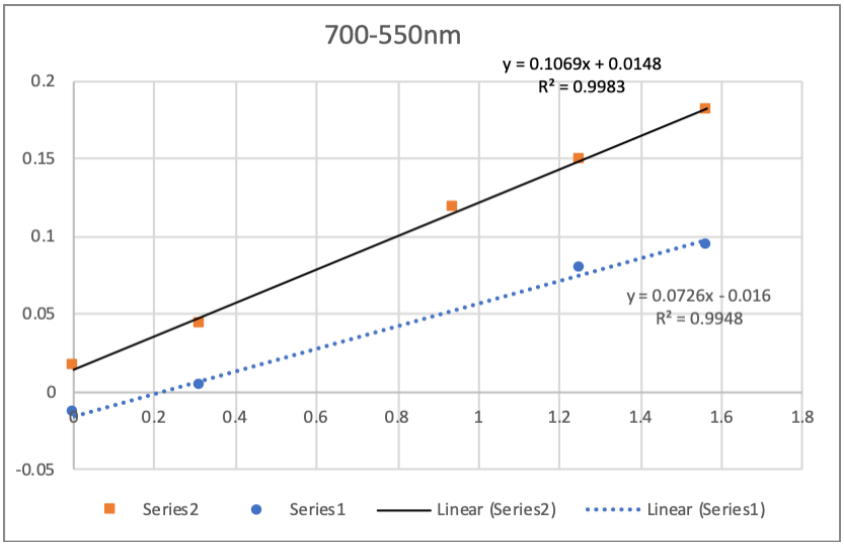

Figure 19: HCl-SDS method one-pump method vs Ruzicka et al. (2019) two pump pFI intercomparison study

Calibration curves from the intercomparison study using 700nm reaction wavelength with a 550nm reference wavelength., (Series-1) Ruzicka et al. (2019) pFI method (blue), with R^2=0.9948 . (Series-2) HCl-SDS µSIA method (orange, this work), R^2=0.9983. Y-axis is absorbance (AU), X-axis is p concentration in µM PO_4.

Chapter 3. System Design

Prior to development, no commercially produced µSIA system was available that could operate in an unattended oceanic environment. As such, each subsystem had to be either developed or optimized for this purpose, these include the µSIA manifold (Ch. 3.1), the control system(Ch. 3.2), the power supply (Ch. 3.3), the protocol sequence (Ch. 3.4), the mounting system (Ch. 3.5), and the housing (Ch. 3.5). In this chapter we describe each subsystem to provide a blueprint for further development. First, the µSIA manifold consists of a number of physical components which act together in order to perform the reagent-based assay. The disparate manifold components require communication in order to act in concert, for which a software control system was developed. Providing power to the control system necessitated the development of a power system. To accommodate the uncertainty of in-situ sampling, calibration and cleaning protocols were standardized to handle potential problems from bubble introduction to the system, filter clogging, residue formation, and degassing. Finally, custom housing and mounting platforms were developed to protect the electrical equipment from the environment.

3.1 µSIA Manifold

The µSIA System (Figure 1 and Figure 20) consists of two multi position valves (MPV, VICI®), a syringe pump (Cavro® XCaliber Modular Digital Pump), spectrophotometer (Ocean Optics Flame-T-UV-Vis spectrophotometer, working range ~400-850nm), and light source (LS-1-LL model Tungsten Halogen Light Source). Tubing was Teflon™ FEP Resin Tubing with an internal diameter of 0.75mm.

The primary MPV is a 6 Port VICI valve and actuator that has a commercially available Lab-on-Valve (LoV, Figure 1, Figure 2, Figure 20) mounted on it. The principal

feature of the LoV is the central flow channel that connects the common port (Figure 20) on the LoV to any of the other 6 LoV ports. These six ports are the inputs for the ascorbic acid reagent (AA), mixed molybdate reagent (MO), flow cell apparatus, the common port of the sample MPV, the degas fitting, and the waste line. The common port on the LoV is connected to a 1mL (internal volume) cylindrically wrapped holding coil that is connected on the other end to the syringe pump (Figure 20). The holding coil has the dual function of acting as a reaction vessel while also providing a buffer volume preventing accidental aspiration of the reagents into the syringe pump, which can be damaged by strong acids. The syringe pump is equipped with a 1mL glass barrel syringe and a two-port connector fitting. The connector fitting on the syringe pump connects the glass barrel syringe either to the holding coil or to the carrier solution intake. By rotating the valve, the common port of the LoV can be connected to any of the six ports.

The flow cell consists of a 142mm length of PEEK™ tubing with an internal diameter of 0.75mm (internal vol. = 62.7µL, including dead space the total volume is ~70 µL). Light, from the tungsten bulb, is supplied to the flow cell through a PEEK™ optical fiber. The light transmitted from the flow cell is connected to the spectrometer with another PEEK optical fiber. The two optical fibers are aligned so that they form a straight line with the flow cell. The reacted sample mixture flows from the holding coil through the LoV into the flow cell, and out to a waste line.

The other MPV is the sample selection valve, which is fitted with a Cheminert® Model C25 6 Position Valve head (Figure 20). The common port of the sample valve permits switching between the six ports which are connected to solutions containing different concentrations of PO_4 spiked standards, the waste line, and the sample intake line (Figure 20). Seawater/freshwater samples pass through a Global FIA In-Line Filter Probe equipped with a 25µm (pore size) microporous Teflon tubing filter inlet to the sample intake port. However, aspirating a sample through the filter probe, can result in cavitation, resulting in bubble formation. The introduction of air bubbles into the manifold causes flow inconsistencies and can lead to refractive index problems in the µSIA system. To overcome this problem a fitting was added to the LoV that allowed the sample to be de-gassed before its introduction into the reaction stream. The degas fitting consisted of a simple 5mL plastic

luer-lock syringe (without piston) and a 0.2µm filter (Millipore Sigma, SLFG025LS) on the open end to prevent particulate matter from falling into the syringe, though any covering that allows air to pass through will do. The degas fitting is positioned on the LoV in a vertical orientation to allow gas to escape.

All liquids including reagents, carrier, standards, and waste were stored internally in FLEXBOY® (Satorius AG, FFB102670, FFB102812) sterile ethyl vinyl acetate bags originally designed for blood storage.

3.2 Raspberry Pi Control System

The control system for the Field Deployable µSIA-PO_4 was developed using a Raspberry Pi 3 single board computer with communication between peripherals handled by the Python programming language, version 2.7. Both the valves and pump use the RS-232 serial communication protocol which is provided by the pySerial Python package. The spectrophotometer uses a USB communication scheme which is provided by a C-language application program interface implemented in Python by means of the static compiler Cython package. To minimize power consumption and thus maximize total run time, power supply to the light source, valves, and pump (24V) is toggled off between individual runs by pulling the Vicor DC/DC converters to 0V on the power supply board (Figure 22). The Vicor module is controlled through the Raspberry Pi's general purpose input/output (GPIO) pins by means of the Python Raspberrypi-GPIO package. Data handling is performed using a secure shell network protocol and a combination of the Pandas, Numpy, and Matplolib Python packages, which provide for automated data organization, storage, and processing (appendix 1).

3.3 Power System

Power is supplied to the system by four Blue Robotics 14.8V 18Ah Lithium-Ion Battery Packs (Figure 21). The Raspberry Pi requires a 5V supply and provides power to the spectrometer through its USB connection, while the two valves, pump, and light source require a 24V supply. To accommodate the power requirements of the individual components and provide a steady supply over the course of a field deployment a power supply board was built by the UHM SOEST Engineering Support Facility. The Power Supply Board (Figure 22) placed two sets of two battery packs in series and two of the sets in parallel, yielding a nominal voltage of 29.6V and capacity of 36Ah. DC-DC converters were installed on the power supply board to provide the appropriate voltage to each of the individual components. In total the 4 battery packs provide a theoretical ~7 days of run time.

3.4 Protocol Sequence

The analytical cycle for the determination of phosphate remained the same for all methods developed. An analytical cycle encompasses a determination sequence (Table 3) repeated for each standard and a sample in order to produce a calibration curve to compare the sample against. Each determination sequence consists of six steps: 1. System Flush, 2. Prime Reactants, 3. Establish Baseline, 4. Load Holding Coil with Reactants, 5. Phosphate Determination, and 6. System Cleaning. The light source is turned on 25 minutes prior to running an analytical cycle to allow it to stabilize the light output. All port references are referenced to the valve layout, either LoV or sample, depicted in Figure 20. The Python code for the determination sequence can be found in appendix 1.

3.4.1 System Flush

The first step in each determination sequence is to flush the system. A system flush involves aspirating 1mL of carrier solution into the syringe pump. Then moving the LoV to the waste position (port 4) and dispensing 600µL of carrier through the holding coil and LoV to waste (port 4). The LoV position is then switched to the flow cell (LoV port 2) and the remaining 400µL is dispensed through the flow cell to waste. The carrier is dispensed at the relatively high speed of 200 µL/sec, as a means to dislodge any air bubbles. If the solution to be analyzed is a sample the first step in flushing is to remove the 2.0mL of carrier in the degas fitting by switching the LoV to the degas fitting (port 1) and executing two sequential 1mL aspiration and dispensing steps to flush the material to waste through LoV (port 4).

3.4.2 Prime Reactants

A priming step is required to ensure that the reactants are primed for the loading step by ensuring there is no dead volume where the reagent line connects to the LoV. Additionally, for the AA and MO reagents this step is a preventative measure against back flushing of other liquids from the common port as the LoV rotates between ports.

The priming step involves first aspirating 300µL of carrier into the syringe. Followed by aspirating 30µL of AA (LoV port 6) at 67µL/sec into the holding coil. The position of the LoV is changed to waste (LoV port 4) and the pump dispenses 150µL. This sequence is then repeated for the MO reagent (LoV port 5).

Reagent priming is followed by priming of the solution to be analyzed, either a standard or sample. There are two separate priming sequences one for a standard and one for the sample.

For a standard, 300µL is aspirated from the corresponding port on the sample valve at 67µL/sec into the holding coil on the LoV through port 3. This step is required to

displace carrier that fills the tubing connecting the LoV to the sample valve (LoV port 3 to sample valve common port) between determination sequences (see cleaning step).

Sample priming requires aspirating the sample from the in-line filter probe (sample valve port 1) through the LoV (via LoV port 3) into the holding coil then reversing the flow and dispensing the sample to the degas fitting (LoV port 1). A total of 2.3mL of sample is aspirated through the filter, and is accomplished in three steps of 0.5, 0.9, and 0.9mL, as the syringe pump only has a capacity of 1mL. Aspirating through the filter at any speed causes cavitation and thereby air bubble formation and introduction to the manifold. Through experimentation it was found that aspirating 1.4mL total through the filter (sample valve port 1) at a rate of 20µL/sec, we could recover between ~1.0-1.2mL of the sample. As the volume of air introduced is relatively predictable, standardized cleaning and air flushing protocols were developed to eliminate interference within and between determination sequences. The first 0.5mL of aspirated sample is used to prime the tubing between the filter and the LoV. This is followed by 1mL of carrier flushing of the holding coil to the waste (LoV port 4). The second 0.9mL of sample is aspirated into the holding coil, the flow is then reversed and 0.7mL is dispensed to the degas fitting (LoV port 1). This is repeated for the third 0.9mL step, both the second and third steps are followed by a 1mL carrier flush of the holding coil to waste (LoV port 4).

3.4.3 Baseline Determination

The baseline is determined using the sample/standard before any reagent addition. The baseline determination is the reference against which the reacted sample/standard is measured in the absorbance calculation

Baseline determination is accomplished by aspirating 600µL of the sample/standard through the selection valve into the holding coil, either a sample from the degas fitting (LoV port 1) or a standard from LoV port 3, and dispensing 300µL through the LoV to the flow cell (LoV port 2). The sample/standard is dispensed at 67µL/sec to displace the carrier solution that fills the flow cell between detection sequences. After loading the

flow cell with the unreacted sample, the spectrometer takes 100 light intensity spectra which record the intensity of light at each wavelength that passes through the flow cell. These spectra of the unreacted solution are recorded, processed, and stored for use as the baseline.

3.4.4 Load Holding Coil with Reactants

In the loading step the reagents and sample/standard are loaded in sequence into the holding coil. First 100µL of the MO reagent is aspirated from LoV port 5 at 20µL/sec into the holding coil. Next 50µL of the AA reagent is aspirated from LoV port 6 at 20µL/sec into the holding coil in sequence behind the MO reagent. Finally, 175µL of the sample/standard is aspirated at 20µL/sec, either as a sample from the degas fitting (LoV port 1) or a standard from LoV port 3. The reaction mixture has a total volume of 225µL.

3.4.5 Phosphate Determination

The determination step is accomplished by reversing the flow direction of the pump and dispensing 155µL (except where noted) of the reaction mixture from the holding coil into the flow cell (LoV port 2) at a rate of 10µL/sec. Once the reaction mixture fills the flow cell the position on the LoV is changed from the flow cell port to the waste (LoV port 4), and 1mL of carrier solution is flushed through the holding coil to waste. Changing the valve position isolates the flow cell preventing additional reaction mixture from entering it. Flushing the holding coil and common channel prevents formation of particulate and colloidal PMoB in the manifold, which can lead to carry-over problems and/or flow inconsistency. The spectrometer begins recording the light spectrums as soon as the pump is initialized to begin flushing. The length of time that the spectrometer records is dependent on the particular method employed.

3.4.6 System Cleaning

After the PO_4 determination step concludes the cleaning step starts. First, 1mL of carrier is flushed through the flow cell (LoV port 2) to waste displacing the reaction mixture. Next, if the solution to be measured is a standard, 1mL of carrier is dispensed to the waste port on the sample valve (sample valve port 2) through LoV port 3. This is done in order to displace the standard that fills the LoV-sample valve tubing. If the solution is a filtered seawater sample, 1mL of carrier is again flushed to the sample valve (via LoV port 3) to the filter (sample valve port 1) instead of the waste port (sample valve 2). This displaces the previous sample from the lines and back flushes the filter to prevent clogging.

An additional cleaning step for the degas fitting on the LoV is required for a filtered sample. The additional step removes the remaining sample from the degas fitting and fills it with DI. Filling the degas fitting with DI dissolves any salt residue left on the walls of the syringe. Since the volume of the remaining sample in the degas fitting is unknown 700µL is aspirated from the degas fitting (LoV port 1) to the holding coil. The aspirated 700µL ensures that all remaining sample is removed from the degas fitting, but this step introduces air bubbles to the µSIA system. The air bubbles and remaining sample in the holding coil are then flushed to waste (LoV port 4), followed by another 1mL of carrier. Finally, a total 1.9mL of carrier is aspirated and dispensed to the degas fitting (LoV port 4) sequentially in 1.0 and 0.9mL steps. Carrier is left in the degas fitting until the next filtered sample determination.

3.5 Housing and Mounting

Development of the Field Deployable µSIA-PO_4 Auto Analyzer required the design of housing and mounting platforms. Initially a housing suitable for use on a dock was developed and using this experience a more substantial water-proof housing suitable for

ocean deployment was constructed. The water proof housing and corresponding mounting were constructed by the UHM SOEST Engineering Support Facility.

3.5.1 Dock Based Housing

Dock based operations were accomplished by placing the μSIA system in an Action Packer® (Rubbermaid) covered with a waterproof tarp with the filter probe placed in a 1.5L Nalgene container. This 1.5L container was filled using a peristaltic pump that continuously pumped seawater from the sampling area into the container which overflowed thereby producing a continuous flushing of the container contents (turnover time = 2.5min,
Figure 23).

3.5.2 μSIA Mounting within Waterproof Housing

A removable mounting platform that fit inside the housing was constructed from a single sheet of aluminum. The mounting platform consists of three vertical bulkheads at 120° angles (Figure 24). The three-bulkhead system was devised to maximize the mounting surface area while minimizing total volume. The bulkheads also served to separate the housing interior into three separate sections: containing different parts of the system: electrical components, μSIA and LoV, and reagent (Figure 25, Figure 26, Figure 27).

The electrical section housed the pump, valve motors and actuators, the Raspberry Pi, power control board, and a serial-USB adapter hub. The μSIA section housed the active μSIA components: pump and valve heads, light source, and spectrometer. The reagent storage section housed the reagents, standards, carrier, and liquid waste bags. The four battery packs were distributed between the three sections.

Small (1-2cm diameter) bulkhead pass-throughs between the sections were provided for reagent lines, power supply wires, and for the battery mounts. Larger

bulkhead pass-throughs were required for the μSIA hardware to straddle the wet chemistry side and electrical side (Figure 24). The light source and spectrometer were mounted inside the wet chemistry section in order to accommodate the optical fiber. The reagent storage section had a mounted cross bar which served to hang the reagent, standard, and waste bags (Figure 27).

3.5.3 Waterproof Housing

This housing (Figure 28) was constructed from a 76.2cm length of PVC tubing (external diameter 34.3cm, internal diameter 29.2cm) with end caps made of high-density polyethylene (top) and polycarbonate (bottom). The total internal volume of the package was 70.4L giving it a buoyancy of ~72kg for seawater. The bottom ~5cm of the internal space in the housing was used for weights, as the dry weight of the package is ~40kg. One lead and one steel plate provided ~27kg leaving the package with a positive buoyancy of ~5kg. ~6.8kg of additional weight was secured to the outside of the housing to make the entire package negatively buoyant. A single pass-through in the top endcap provided the inlet for the external sample introduction to the μSIA system. A small protective housing for the filter probe was constructed and attached to the side of the housing using a series of zip ties. Teflon™ tubing connected the filter probe to the inlet pass-through. The connecting tubing and inlet were protected by running the connecting tubing through a length of Tygon® tubing and a 3.8cm high aluminum ring mounted to the top endcap (non-penetrating screws).

Table 3: Determination Sequence

Step	Action	Method	Valve Position number [LoV]{Sample}
1. System Flush	Flush holding coil (HC)	Dispense carrier 1mL at 200µL/sec (for all carrier dispense) to waste	[4]
	If a Sample follows, ready degas fitting	Aspirate 2mL carrier from degas fitting, dispense to waste	[1] [4]
2. Priming Reactants	Prime reagents	Aspirate 30µL AA into HC at 67µL/sec Dispense 100µL AA+carrier to waste Repeat for MO	[6] [4] [5]
	Prime sample or standard	Standard: aspirate 300µL at 67µL/sec, dispense 1mL carrier to waste Sample: Aspirate sample 0.5mL at 20µL/sec, dispense 1mL carrier to waste, aspirate sample 1.8mL, dispense 1.4mL to degas fitting, dispense 1mL carrier to waste	[3]{3-5} [4] [3]{1} [4] [1] [4]
3. Establish Baseline	Determination of target sample/standard baseline light intensity	Aspirate 600 µL of sample/standard to holding coil, dispense 300 µL at 67µL/sec to flow cell	[3(std),1(samp)] [2]
	Trigger spectrophotometer	Acquire 100 light intensity spectrums, take average and write to memory for use as baseline	
4. Load Holding Coil	Load holding coil with reactants	Aspirate each in sequence at 20µL/sec: *1.* MO 100µL [5] 2. AA 50µL [6] 3. Analyte175µL	[5] [6] [3(std),1(samp)]
5. Phosphate Determination	Determination of sample/standard	Dispense 155µL (except where noted) of reaction mixture at 10µL/sec to flow cell	[2]
	Tigger spectrophotometer	Acquire light spectrums of reaction mixture in the flow cell for X sec (time dependent on method). Combine with baseline data and process for analysis	
6. System Cleaning	Prepare for next determination sequence	Flush carrier through holding coil to the flow cell (1mL), sample valve (1mL), and degas fitting [1](1.9mL, if used)	[2] [3]{3(std), 1(samp)} [1]

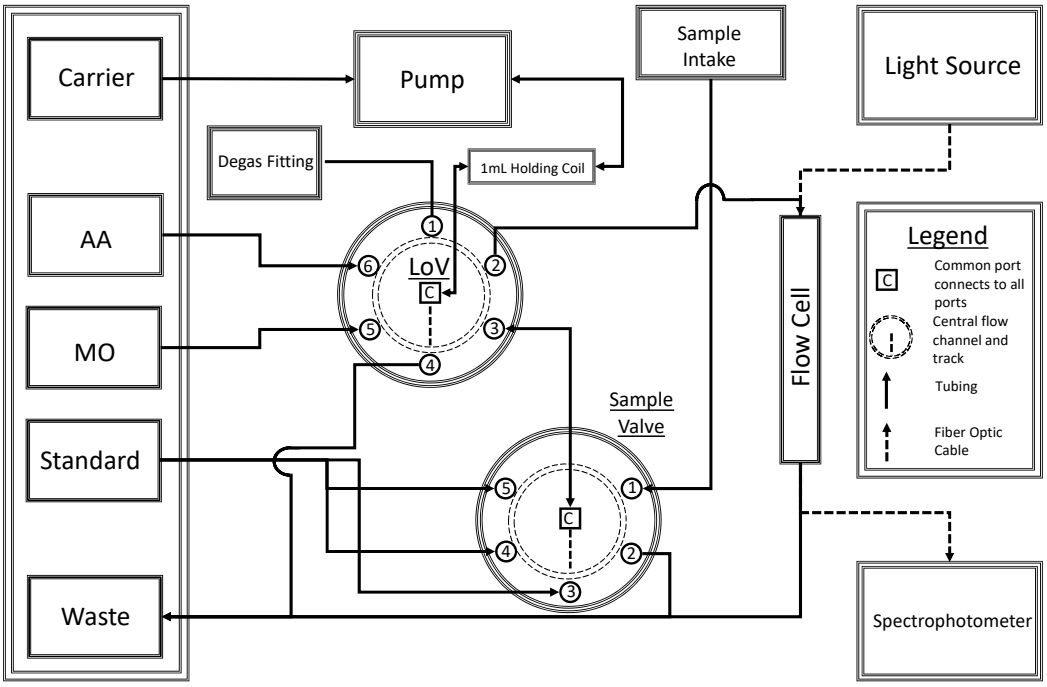

Figure 20: Field deployable µSIA auto-sampling system schematic

Schematic of the field deployable µSIA auto-sampling system showing tubing connections between various parts with reagent bags displayed on the left-hand side as boxes. For the benefit of readability, the three standard bags are combined into a single box on the left-hand side. All waste lines as well as the outlet from the flow cell connect to the same waste bag. Both the sample valve and LoV show the port number connections as well as the common port (C). Dotted lines are used for fiber optic cables to distinguish them from liquid carrying tubing.

Figure 21: Blue Robotics battery pack

Blue Robotics 14.8V 18Ah Lithium-Ion Battery Pack designed for use in the BlueROV2, SKU: BATTERY-LI-4S-18AH-R3-RP (bluerobotics.com).

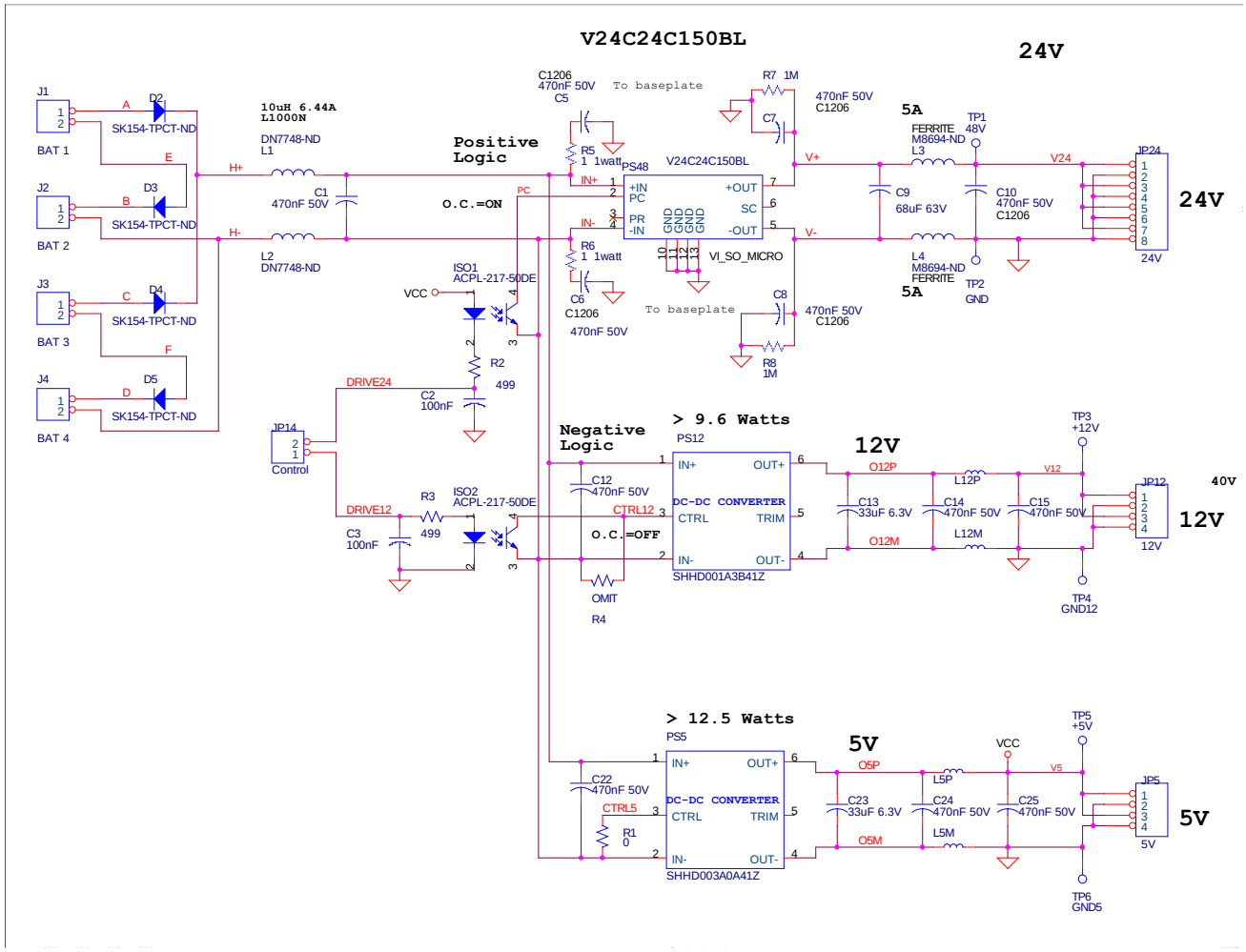

Figure 22: Power supply diagram

Schematic of the power supply board designed by the UHM SOEST Engineering Support Facility

Figure 23: Dock based mounting and housing platform

Dock Based mounting platform (left) which was placed inside the action-packer housing (right) during operation with laptop removed and covered by a plastic tarp for added water resistance. The sample intake filter for the auto-sampler was placed inside the Nalgene bottle secured in place by a cinder block. Sample was continuously pumped from the sampling area below by an external pumping system (located behind the auto-sampler) into the bottom of the Nalgene container thereby creating a turnover of the contents.

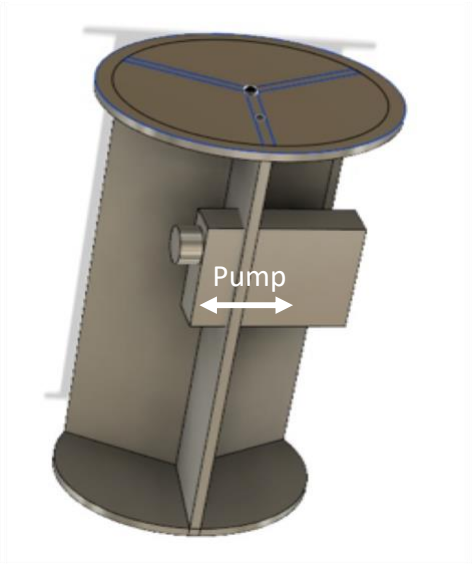

Figure 24: Auto-sampler water-proof mounting platform 3D model

3D model of the water-proof mounting platform showing a bulkhead pass-through of the syringe pump bridging the µSIA section from the electronic section.

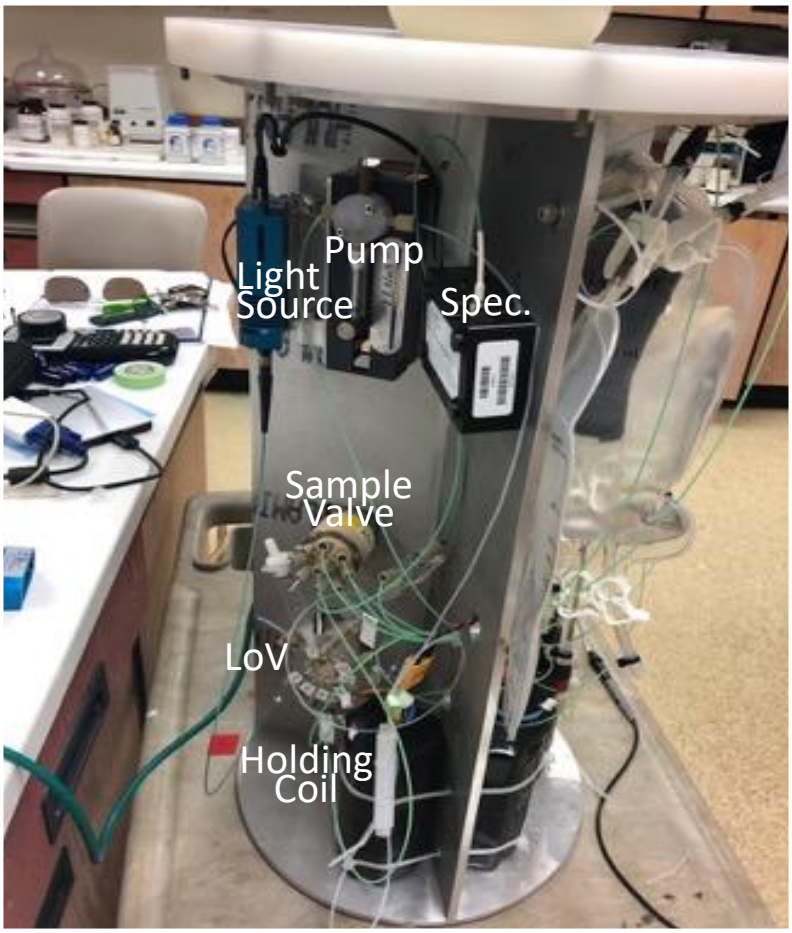

Figure 25: Water-proof mounting platform wet-chemistry section

Internal arrangement of μSIA components in the wet chemistry section of the ocean deployable system: light source, syringe pump, spectrometer, sample valve, LoV, and Holding coil.

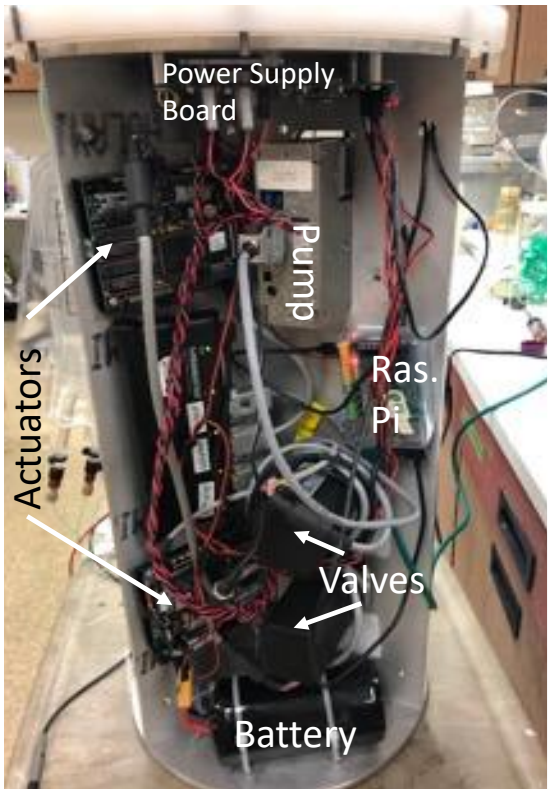

Figure 26: Water-proof mounting platform electrical section

Internal arrangement of the electrical systems section of the water-proof mounting platform: actuators, power supply board, pump, raspberry pi, valves, and battery.

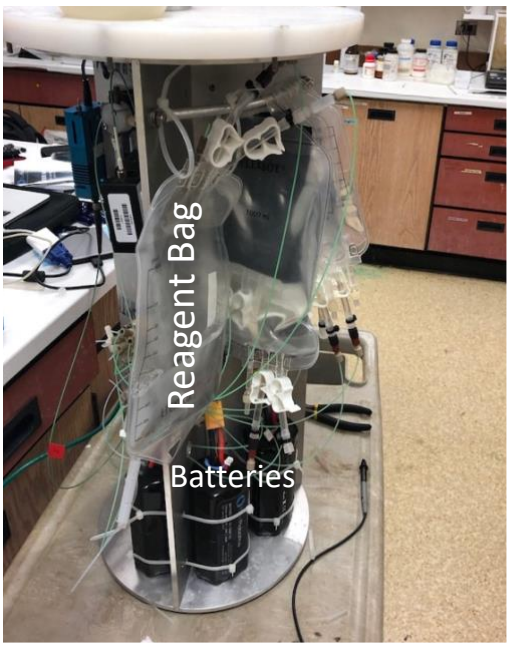

Figure 27: Waterproof mounting platform reagent storage section

Internal arrangement of the water-proof mounting platform reagent storage section. Reagent bags are shown hanging from the cross-bar at the top, the waste bag is positioned so the connection faces up to allow waste to flow easily into the bag, while the rest of the bags have their connections facing down to allow reagents to easily flow out.

Figure 28: Waterproof housing

Waterproof Housing immediately prior to deployment. The filter probe with protecting housing, tubing, and aluminum inlet can be seen attached to the side.

Chapter 4. Results and Discussion

In order to demonstrate viability of the proof-of-concept for a flow based in-situ monitoring system a number of tests had to be performed. What follows in this chapter is a series of experiments designed to test the practical operation of the field deployable PO_4 analyzer.

In-situ continuous autonomous applications carry with them a number of inherent constraints that differ from those of lab-based systems and methods. The constraints stem from the need to encapsulate sufficient resources for operations that substitute for those provided in a laboratory setting. The resources provided in a laboratory setting include access to mains electricity, unlimited reagent and carrier volumes, access to waste disposal, large stable benchtop space for instrumentation, temperature control, replacement parts, and the ability for physical inspection during operation. These constraints required the development of a robust protocol method, chemical assay, mounting, and housing.

4.1 Salinity Effects

In addition to fresh water and open ocean applications with constant salinity, estuarine and river mouth environments are of particular scientific and environmental importance. Continuous monitoring of nutrients in these areas could provide an early warning of elevated nutrient fluxes to coastal areas. Additionally, the time stamped datasets would be invaluable for understanding the resulting environmental responses. The issue with these areas is that they experience daily tidal fluctuations in salinity, and thus require a method that is unaffected by changes in salinity.

The influence of salinity on the PMoB chemistry is well noted in the literature but is not uniform for all PMoB methods (Nagul et al. 2015). In order to deploy in an area with

variable salinity an investigation into the effect of salinity on the different surfactant-based reagent assays was conducted. The investigation was conducted in the laboratory by comparing the calibration curve slopes and reaction rates of PO_4 spiked standards in both DI and seawater (SW). The protocol methods are outlined in Ch. 3.4, and the respective reagents described in Ch. 2.4.

4.1.1 H_2SO_4-Brij method

The reaction progress curves of PO_4 spiked SW standards using the H_2SO_4-Brij method were different from those of DI (Figure 29). The differences in both the rate the reaction progresses and the general shape of the reaction curve (Figure 29) made comparisons between the DI and SW calibration curves difficult. The difference is a result of the shift in the absorbance spectrum from the single peak at 760nm to the dual peak spectrum at 710 and 880nm as described in Ch. 2.6, and how it relates to the nature of the PO_4 complex in the different ionic mediums. The rate of the seawater reaction is quicker than that of the DI. Further, the rate for the lower 1.5 µM standard is quicker than the 3.0 µM standard. The overall shape of the reaction curve for the 1.5 µM seawater standard is similar to that of corresponding DI standard, but not for the 3.0 µM standard. The 3.0 µM seawater standard does experience a smooth increase in absorbance prior to the decrease corresponding to the shift in spectrum shape. Instead, the 3.0 µM seawater curve experiences a similar phenomenon to that of the HCl-SDS method (Figure 15), with a quick initial rise followed by a shallower sloped continued increase. Unlike the HCl-SDS reaction curve, the secondary increase observed for the H_2SO_4-Brij 3.0 µM seawater standard is not linear. We were unable to produce linear standard curves for seawater standards using the H_2SO_4-Brij method and thus determined that it is unusable for in-situ operations.

4.1.2 H_2SO_4-SDS Method

For the H_2SO_4-SDS method, a 410sec data collection window and 515nm reference wavelength was used for construction of the calibration curves (n=3) shown in Figure 30. The main difference that can be observed between the PO_4 spiked DI and SW standards is the initial rate of the reaction. As Figure 31 shows the initial rate of reaction for SW standards is slightly slower than that of DI based standards. The difference in reaction speed can be negated by employing a reaction time of ≥400s, after which the SW and DI absorbances converge to the same value (Figure 31). The result of the long reaction time produces identical calibration curves for DI and SW standards (Figure 30).

The ≥400s reaction time for the H_2SO_4-SDS method presents a few problems with regard to in-situ applications. The most obvious is in the reduction of sampling rate. As described above, each analytical cycle (3 standards and 1 sample) requires a calibration curve be produced. Adding the analysis step (≥400s) to the time it takes for the other steps (system flush, priming, etc.) brings the determination sequence to ~500s. This means that each analytical sequence (minimum 4 determination sequences with 25min lamp warm up) takes ~1hr to accomplish. During the ~1hr, both the lamp and micro-controller are drawing power from the batteries, leading to shorter deployment times. Additionally, long reaction times can cause deposition of residue outside of the flow cell from non-optimized reagent concentrations as a result of mixing issues inherent to all µSIA methods. The residue can build up in the system and lead to problems related to mixing and carry over between samples.

Despite the drawbacks of the long reaction time, the benefits of being unaffected by salinity make the H_2SO_4-SDS method a viable choice for variable salinity environments.

4.1.3 HCl-SDS Method

The HCl-SDS method contrasts with the H_2SO_4-SDS method in that it provides shorter reaction times but is unfortunately subject to salinity effects as seen with the final

absorbance calculations (Figure 32). Figure 32 and Figure 33 show that despite being linear in nature the calibration curves of DI and SW PO_4 spiked standards are not the same with SW standards producing a shallower calibration curve slope ($slope_{DI}$ = 0.119AU/µM vs. $slope_{SW}$ = 0.089AU/µM).

The HCl-SDS method reaction curve follows 2 distinct phases with a transition between them (Figure 33). The 1st phase being the initial non-linear increase in absorbance, followed by a transition period (Figure 33). The 2nd phase is characterized by linearly increasing absorbance during which, and even during the end of the transition, calibration curves can be produced at any time (Figure 33). Figure 33 shows that the transition from the 1st to the 2nd phase for SW standards takes longer than for DI standards. The result is that linear calibration curves can be produced at any time point following the start of phase 2, ~50sec for DI standards and ~100sec for SW standards (Figure 34).

As described in chapter 2, the slope of the 2nd phase of the reaction curve is linearly corelated to the PO_4 concentration. A comparison of the standard curves derived from the 2nd phase reaction curve slopes for DI and SW PO_4 spiked standards shows no statistical difference between the two (Figure 35). While the 2nd phase slopes appear unaffected by salinity, the phenomenon was not discovered until final data analysis after loss of the equipment. Thus, a comprehensive study was not conducted to investigate the cause. The results of the 2nd phase slope analysis was not taken into account in the deciding which of the 2 methods to use in the different environments (constant or variable salinity). Despite the HCl-SDS method being subject to effects from differences in the salinity matrix, disregarding the results of the 2nd phase slope analysis, the HCl-SDS method is a viable choice for deployment in areas with constant salinity such that PO_4 standards can be made to match the local salinity.

4.2 Reagent Stability

In a laboratory setting reagents are generally made up daily to prevent the effects of reagent degradation. In-situ applications do not allow for this. As such, an investigation was conducted under laboratory settings as to the stability of the H_2SO_4-SDS and HCl-SDS reagents. The investigation was conducted by running each method continuously over a three-day period using seawater spiked standards. The three-day target for stability tests corresponds to ~1/2 of the estimated battery power available for an in-situ deployment. The protocol is described in Ch. 3.4, and the respective reagents for each method are described in Ch. 2.3.

4.2.1 H_2SO_4-SDS Method

For the H_2SO_4-SDS method stability test, an analytical cycle was performed every 3hrs for 60hrs. Absorbance was calculated after a 410sec reaction time averaging the last 5sec. Over the 60hr period, the H_2SO_4(SDS) method exhibits a ~10% drop in absorbance (Figure 36). Figure 37 displays the calibration curve slope and associated R^2 value for each analytical cycle (absorbance values shown in Figure 36) over the 60hr mock deployment. The R^2 value represents confidence in a calibration curve to calculate an unknown concentration in a sample, and for the purpose of this analytical method an $R^2 \geq 0.9975$ represents the bar of confidence as each standard can only be measured once. An $R^2 \geq 0.9975$ conveys that > 95% of the standard deviation of the errors can be explained. That is not to say that a $R^2 = 0.995$ is necessarily unusable, simply a method designed for single determination of both standards and sample requires a high threshold under laboratory conditions.

Figure 37 shows an overall decrease in calibration curve slope steepness, as well as a general decrease in the R^2 calculated for each curve with an increase in erraticism with 75% falling below the R^2=0.9975 threshold. Figure 38 shows the first and last 1.0µM PO_4 SW standard determination sequence in the 60hr stability test. It can be observed from

Figure 38 that after 410sec the first 1.0µM PO_4 SW standard just reaches the zenith of its reaction curve while the final determination sequence has not. This provides an explanation that the drop in absorbance (Figure 36), calibration curve slopes (Figure 37), and erraticism of the R^2 values (Figure 37) is due to the rate of reaction slowing over the duration of the experiment. As the rate of the reaction slows over the course of the experiment, the final absorbance calculation for each standards determination sequence sequentially decreases due to the reaction not completing. Meaning that absorbance calculation is higher than that what was recorded because the reaction curve has not reached the plateau, hence the drop in final absorbance shown in Figure 36 and Figure 38. This drop in final absorbance is then reflected in the drop observed in calibration curve slopes (Figure 37). Further, as the recorded final absorbance values sequentially decrease the R^2 values for the corresponding calibration curves become erratic with a general downward trend. The explanation for the reaction rate slowing is found in the decomposition of ascorbic acid reagent slowing the reduction of the Keggin ion. We will show in Ch. 4.3 that extending the data collection window to ~600s counters the slowing reaction rate.

Finally, the system as a whole displayed the self-cleaning protocol described in the determination sequence (Ch. 3.4). A drop in the absorbance for the 1.0uM standard at the 39hr analytical cycle can be seen in Figure 36. This sharp drop in absorbance is most likely due to a bubble being introduced to the system. As the following determination sequence was not affected, it can be inferred that the system flushing and cleaning steps of the protocol sequence are sufficient to eliminate such problems.

4.2.2 HCl-SDS Method

For the HCl-SDS method stability test, an analytical cycle was performed every 4hrs over a 60hr period with data collection after 200s in each determination sequence. Over the course of the experiment the HCl-SDS method experienced a ~5% decrease in final absorbance from decomposition of the ascorbic acid (Figure 39). The 5% decrease in

absorbance is reflected in the slope of the individual analytical cycle calibration curves (Figure 40). Figure 41 shows the first and last determination sequences of the 60hr stability test for the 1.0 and 2.0µM PO_4 SW standards. While there is an overall retardation of the reaction speed, the rate at which it slows is proportional to the amount of PO_4 in the sample. The observed decrease in the analytical cycle calibration curve slope and absorbance values is not reflected in the corresponding R^2 values, with 85% of the R^2 values above the R^2=0.9975 laboratory threshold (Figure 40). Only the final two calibration curves that fall below the threshold which can be corrected for by increasing the reaction time. This indicates that while the decomposition of the ascorbic acid is a factor, the decomposition affects different PO_4 concentrations at a proportional rate (Figure 40). This further indicates that reagent degradation during the 60hr stability test does not affect the 2nd phase reaction curve slopes (see Ch. 4.1.3). To demonstrate the stability of the HCl-SDS method Figure 42 shows a calibration curve produced by averaging all the analytical cycles (n=12). The result is that the limit of detection for the full 60hr experiment is in line with previous findings (LOD=25nM, Figure 42) even with the ~5% decrease in absorbance. The stability test for HCl-SDS method shows that it is suitable for longer term deployments.

4.3 Dock Deployment

A dock-based deployment was performed using the H_2SO_4-SDS method over a three-day period from 6/15/18-6/18/18 in the Hawaii Kai marine embayment. Hawaii Kai marine embayment is located on the south-east coast of Oahu (Figure 43). The bay receives freshwater inputs from a number of streams derived from orographic rainfall along the ridge and valley system that flank it. Typical PO_4 concentrations in the bay range from 0.1-1.0µM (Anchor, 2011).

The H_2SO_4-SDS method was selected over the HCl-SDS method due to the variable salinity found in the bay. The instrument performed an analytical cycle every 3hr using the

protocol described in Ch. 3.4. Reaction times for the analysis step were extended to 600sec to counter the decrease in reaction speed observed during the stability test.

Figure 44 shows the absorbance values for each determination sequence in each analytical cycle, both standards and samples. The calculated PO_4 concentrations for the filtered samples (Figure 45) show an initial elevated concentration of PO_4 followed by a steady range of PO_4concentrations between 0.05-0.25µM. The elevated initial concentration may be a result of a contamination introduced during the initial set up for the deployment, though it is still within the typical reported range for the bay and rain was observed in the valley during setup. The negative trend in the calibration curve slopes observed during stability tests is also observed here (Figure 46). Despite the negative trend in the calibration curve slopes, the linearity and agreement (R^2) is maintained with 95% of the R^2 values above the R^2=0.9975 threshold (Figure 46). This is a result of the extended reaction time from 410sec to 600sec allowing each reaction to reach the plateau. The increase in reaction time effectively counters the erraticism observed in the R^2 during the stability test (Ch. 4.2.1) due to reduction in reaction speed from decomposition of the ascorbic acid reagent. Towards the end of the 60hr deployment the rate at which the calibration curve slopes decrease displays an increase. This indicates that adding additional time to the method may be needed and potentially the addition of time to the reaction with each successive analytical cycle would be beneficial. In total the field deployable PO_4 auto-analyzer performed well during the dock deployment.

4.4 Laboratory Tank Submergence Test

Two submergence tests were performed with the field deployable PO_4 analyzer. The tests were performed in the UHM SOEST Engineering Support Facility by submerging the equipment in a tank filled with tap water ~21°C. The first test was a leak test of just the water-proof housing without the µSIA components to confirm that the housing cap was airtight. The second was an overnight deployment with an analytical cycle performed once

every 4hr. The deployment employed the HCl-SDS method using a 710 and 515nm wavelengths and a 200sec reaction time. The tank was filled immediately prior to submergence and was not equilibrated to the ambient temperature. Standards were made using LNSW spiked with PO_4 to concentrations of 0.0, 0.5, and 2.0µM PO_4. The external filter probe was placed in an 2L bottle (not submerged) of unfiltered LNSW sample spiked with PO_4 to a concentration of 2.25µM. The unfiltered LNSW used for testing the filtration process were made up 2 hours prior to submergence and thus had time to equilibrate to ambient temperature. Further lab testing was not performed as the cap of the water-proof housing was not designed for repeated sealing.

Figure 47 shows the absorbance values for each SW standard (blue: blank, orange: 0.5µM, green: 2.0µM) and the filter probe (red). The individual calibration curve slopes calculated from each analytical cycle and corresponding R^2 are displayed in Figure 48. Both Figure 47 and Figure 48 show a slight increase in absorbance and slope. One potential explanation is that this could be a result of the temperature of the water filling the tank warming as it equilibrated with the ambient temperature increasing the rate of the reaction. The average calibration curve across all three analytical cycles is shown in Figure 49. Despite the slight increase in slope, the limit of detection calculated by averaging all three analytical cycles (LOD = 29nM P) remains in good agreement with previous HCl-SDS tests. The individual calibration curve slopes for each analytical cycle were used to back calculate the PO_4 concentration in the unfiltered SW sample. Figure 50 shows the result of the back calculation. The mean across all three runs is 2.26µM with a standard deviation of 44nM.

4.5 Field Deployment

A final field deployment was undertaken at the Ala Wai Offshore Observatory mooring station (Figure 51) on the south shore of Oahu. The location was selected for its proximity to the outlet of the Ala Wai canal. The canal serves as the primary drainage

conduit for the heavily urbanized central and east Honolulu watershed. The deployment was planned for three days at a depth of 1ft and a sampling frequency of 3hr. The HCl-SDS method was chosen for this deployment.

The field deployable PO_4 analyzer was positioned to rest between the main frame and the vertical pole on the cross bar connecting the frame to the outside ring of the mooring. The bottom was positioned rest on both the cross bar and the outer ring. The sides and bottom of the instrument were secured and immobilized by a series of 25 industrial grade 45in 175lb nylon zip ties and 3 ropes of varying length. Unfortunately, the instrument was no longer attached to the mooring at the end of the experimental period, so no data were available to evaluate the system.

4.6 Discussion and Recommendations for Future Work:

Overall it was the component and material constraints, not the constraints related to in-situ operation, that played the largest roll in the development cycle. Spectrometer availability limited the wavelengths available for use, limiting analysis to the lower 710nm absorbance peak. Pump availability dictated the use of a single pump constraining the FI technique employed in the project to a µSIA system. As mentioned in Ch. 1.8 µSIA differs from batch, CFA, FI, and pFI techniques in that µSIA does not provide for good mixing between sample and reagents. This problem is of particular relevance in multiple reagent assays and is further complicated by density differences between reactants. Contending with the complex mixing regime resulted in longer development time for each chemical assay presented here. Contending with the limited construction materials necessitated creative solutions. For example, during construction of the waterproof housing lead was used to calculate the additional internal space needed for weights to make the package negatively buoyant. Due to material constraints the correct amount of lead was unavailable requiring the supplement of steel. The lower density of the steel left the package with a positive buoyancy necessitating external weights. The imbalance between the positive

buoyance of the instrument, and the negative buoyance of the exterior weights coupled with continuous wave action allowed the instrument to work its way up and out of the double barrel hitch knot that secured its bottom and sides (Figure 28).

Despite the loss of the field deployable PO_4 auto-analyzer, the project as a whole was successful. In total, two PMoB µSIA methods were developed, both the H_2SO_4-SDS and HCl-SDS methods presented are recommended for further use. The main benefit of the H_2SO_4-SDS method is that it appears to be unaffected by changes in salinity, making it a good choice for variable salinity deployments. Though, the H_2SO_4-SDS method suffers from a longer reaction time, lower calibration curve slope, and higher LOD than the HCl-SDS method. Extending the reaction time from 410sec to 600sec was effective in countering the effects of decomposition observed in the ascorbic acid reagent as noted in Ch. 4.2.1. The HCl-SDS method in contrast, analytically outperforms not just the H_2SO_4-SDS method but the Ruzicka et al. (2019) that it is based on when comparing calibration curve slopes and LOD (Figure 18 and Figure 19). While the HCl-SDS method suffers from a salinity effect when looking at absolute absorbance, 2nd phase slope analysis may overcome this drawback with further development.

With the exception of the syringe pump, all the materials used in the construction of µSIA manifold are recommended for further use thanks to their robust design and extensive developer documentation. The syringe pump suffers from the necessity to fill the syringe prior to dispensing any liquid, dealing with this constraint adds unnecessary movements and time to the protocol sequence. Note that a spectrometer with the capability to measure at 880nm would be beneficial as this would enable analysis of the higher of the two absorbance peaks.

The protocol sequence developed performs well in handling the chaotic nature of the in-situ environment (bubble introduction, temperature changes, etc.) and is recommended for use in future projects. The use of a Raspberry Pi in the control system is ideal for development purposes thanks to its ease of use and beginner friendly documentation, though if a production grade system is ever developed there exist a host of more robust micro-controllers with better performance and less computational overhead. The results of the dock-based deployment demonstrate the viability of the µSIA technique for in-situ applications. In addition to PO_4 determination, it shows that any flow-based method could

be adapted to this system and deployed alongside either of the PMoB methods presented here.

In the iteration of the field deployable PO_4 analyzer described in this document the author offers no recommendation for further use, outside of a proof of concept. Batch, CFA, FIA, and pFI techniques all provide for better mixing than μSIA, with pFI offering the ideal technique for this purpose (Ruzicka, 2016). Further, sequential addition of reagents adds unnecessary complexity to the protocol sequence by having to keep track of syringe volume.

If rebuilt a number of changes could be made to improve the system, with the addition of a second pump being the most beneficial. Programable flow injection is a far superior technique to μSIA (Ruzicka, 2016). The addition of a second pump allows the introduction of confluence points to the manifold, achieving 100% mixing between reagents. This would have the benefit of a reduction in development time by optimization of the reaction concentrations and reduction in reagent use. Use of an LED light source would further reduce energy usage and increase the sampling rate by cutting the 25min tungsten-halogen lamp warmup time. An LED lights average power consumption is ~8W whereas the tungsten-halogen LS-1-LL light source used in this work consumes ~90W. The addition of a solar unit would further extend the total runtime. While the addition of a second pump would increase the energy usage, the reduction in reaction time coupled with energy savings from LED's and a photovoltaic panel would more than offset it.

Additional optimizations include replacing the syringe pump with a milliGAT pump (GlobalFIA), at half the size and built in actuator control module it would greatly cut down on space. The LOV and sample valve are never operated at the same time, size reduction could be achieved if they could share a single actuator control module. A major size reduction could be made with a custom liquid storage solution that minimizes dead space as the current blood storage bags are designed with other considerations in mind and are not efficient for storage in a confined space. The blood bags are designed to hang vertically with long protruding inlets and is how they were employed in this design. If rebuilt packing the liquid storage bags flat on top of each other would be an efficient use of space reducing their total space consumption by ~1/2. Finally, much of the size of the current iteration is a result of having to place components according to the housing. As mentioned above, the

budget for the housing was insufficient and did not permit for materials or exterior design. Thus, the interior components had to be placed based on the dimensions of the container. Form should always follow function instead of the other way around, and a custom housing built from the ground up with space optimization in mind would bring a drastic reduction in size.

If rebuilt with the recommendations provided above, it is the authors opinion that the resulting instrument would provide an exceptional platform for long term high quality scientific analysis.

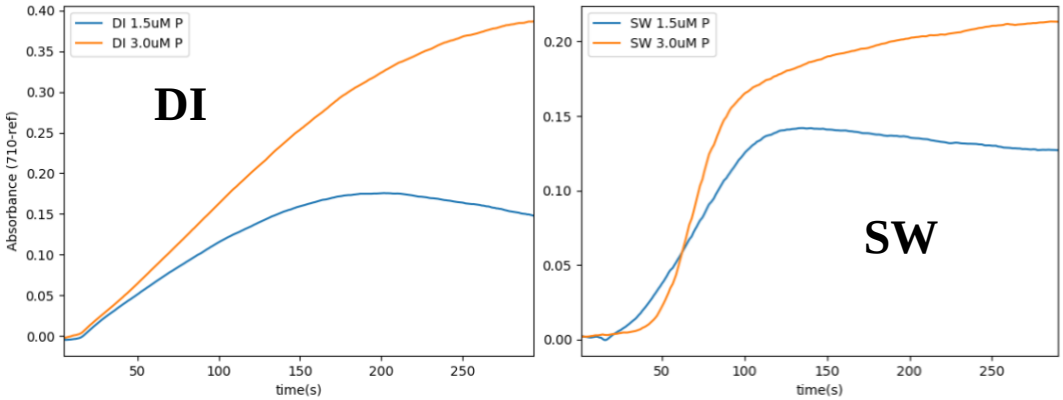

Figure 29: H_2SO_4-Brij method DI vs SW standard reaction curve comparison

Comparison of the H_2SO_4-Brij method reaction curves for the (Left) DI based and (Right) SW based standards with PO_4 concentrations of 1.5µM (blue) and 3.0µM (orange). All reaction curves acquired using 710nm for the reaction wavelength with a 515nm reference wavelength over a 300sec reaction time.

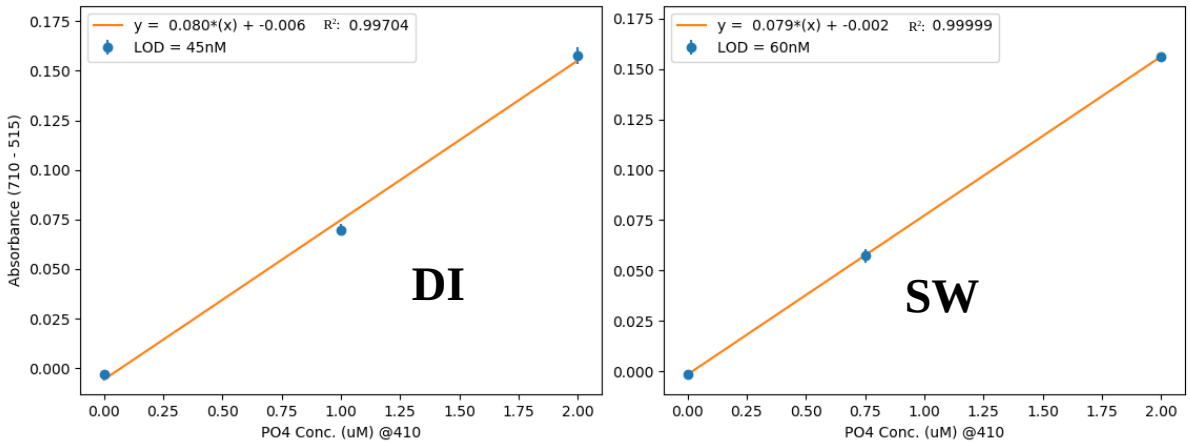

Figure 30: H_2SO_4-SDS method DI vs. SW calibration curve comparison

Calibration curves generated using PO_4(µM) spiked DI (Left) and SW (Right) standards using the H_2SO_4-SDS method with a reaction window of 410s. Each data point (n=3) was acquired using 710nm for the reaction wavelength and a reference wavelength of 515nm.

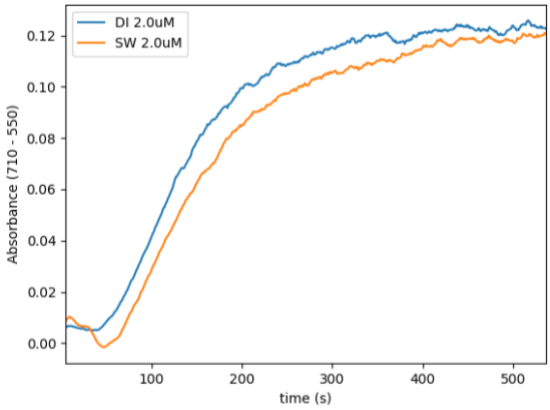

Figure 31: H_2SO_4-SDS method DI vs SW reaction curve comparison

H_2SO_4-SDS method comparison between 2.0µM PO_4 spiked DI standard (blue) and SW (orange). Reaction curves acquired using 710nm for the reaction wavelength with a 550nm reference wavelength over a 530sec reaction time.

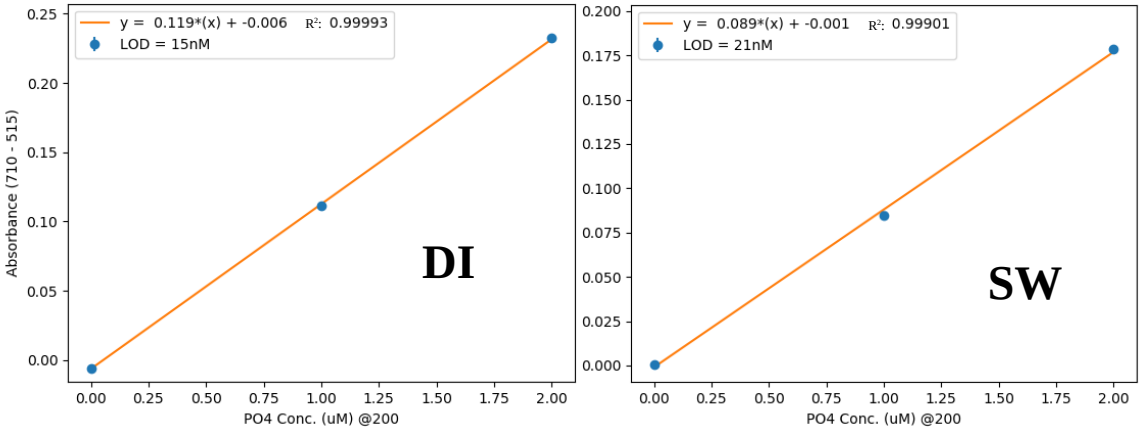

Figure 32: HCl-SDS method DI vs. SW calibration curve comparison

Calibration Curves generated using PO_4(µM) spiked DI (Left) and SW (Right) standards using the HCl-SDS method with a reaction time of 200sec. Each data point (n=3) was acquired using 710nm for the reaction wavelength and a reference wavelength of 515nm.

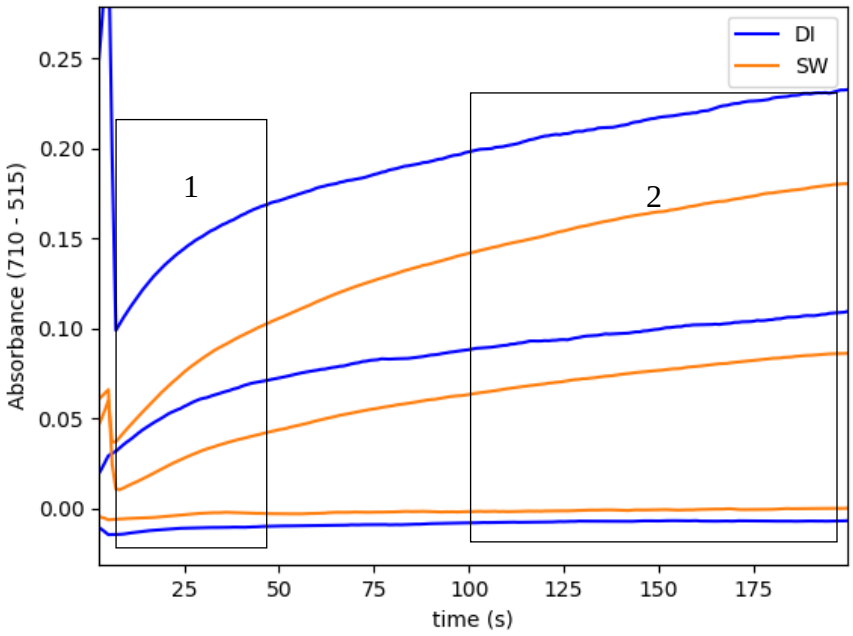

Figure 33: HCl-SDS method DI vs SW standard reaction curve comparison

HCl-SDS method comparison between 0.0, 1.0, and 2.0µM PO_4 spiked DI standard (blue) and SW (orange) over a 200sec reaction time. Using a 515nm reference wavelength. Each curve was acquired using 710nm for the reaction wavelength and a reference wavelength of 515nm. The 2 phases of the HCl-SDS method reaction curves are shown in boxes.

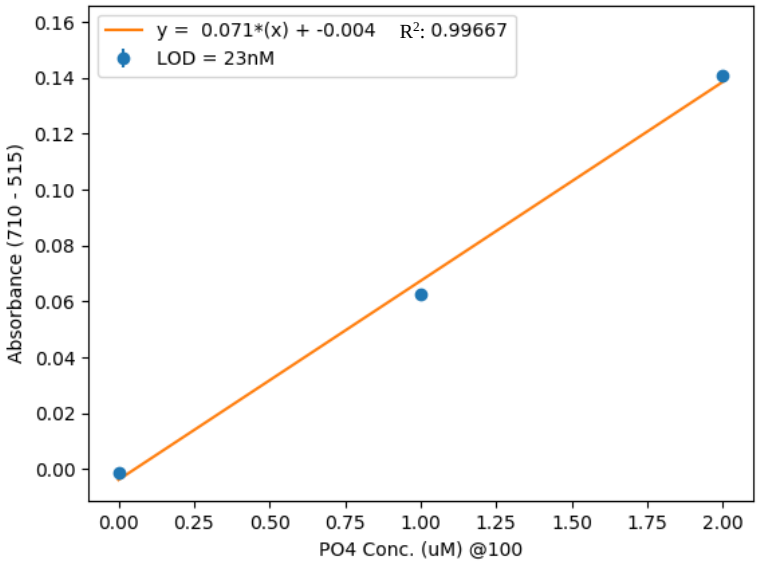

Figure 34: HCl-SDS method SW calibration curve

Calibration curve of different PO_4(µM) spiked SW standards (n=3 for each data point) obtained using the HCl-SDS method. Absorbance values obtained using 710nm for the reaction wavelength with a 515nm reference wavelength with a 100sec reaction window. The LOD obtained for the method is 23nM PO_4 with an R^2 of 0.9967.

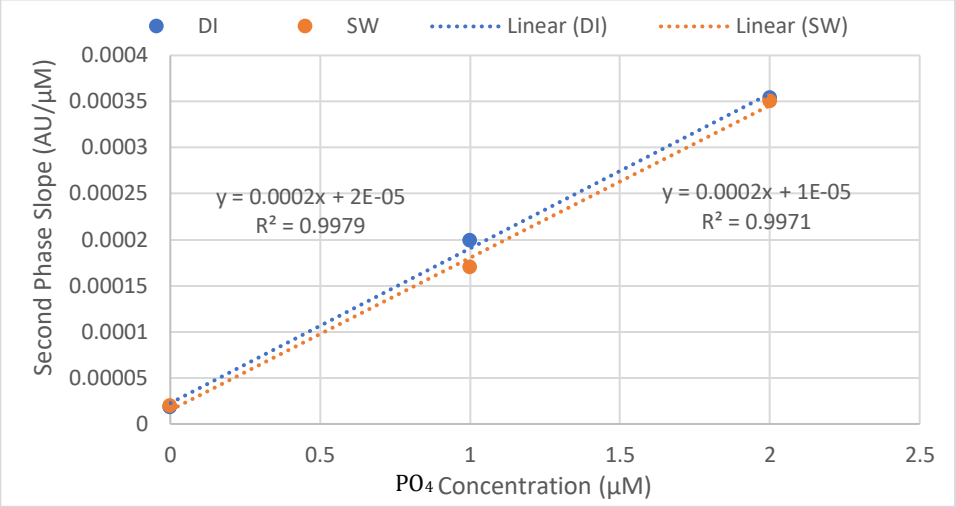

Figure 35: HCl-SDS 2nd phase slope calibration curve DI vs. SW comparison

HCl-SDS method 2nd phase slope comparison between DI(blue) and SW(orange) PO_4(µM) spiked standards, the y-axis is unitless. Each point obtained by calculating the slope of the reaction curve between 175-195sec. Absorbance values from the reaction curves obtained using 710nm for the reaction wavelength with a 515nm reference wavelength.

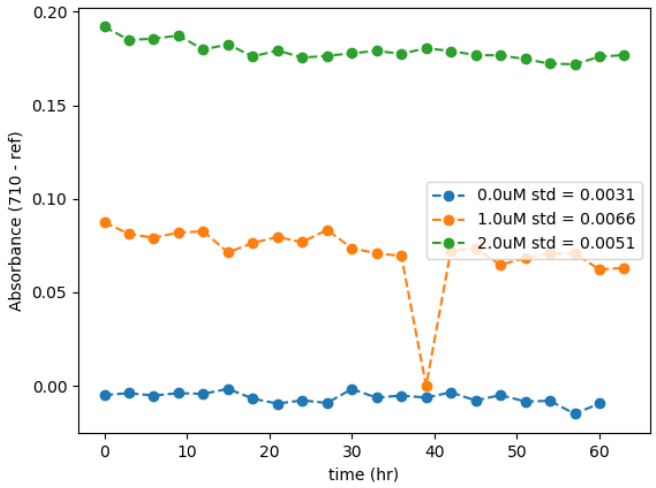

Figure 36: H_2SO_4-SDS method stability test absorbance values

Absorbance values for each standards determination sequence of the H_2SO_4-SDS method stability test. Absorbance values calculated using a 410sec reaction window with a 710nm reaction wavelength and a reference wavelength of 515nm. Standard deviations are calculated for each standard over the full 60hrs.

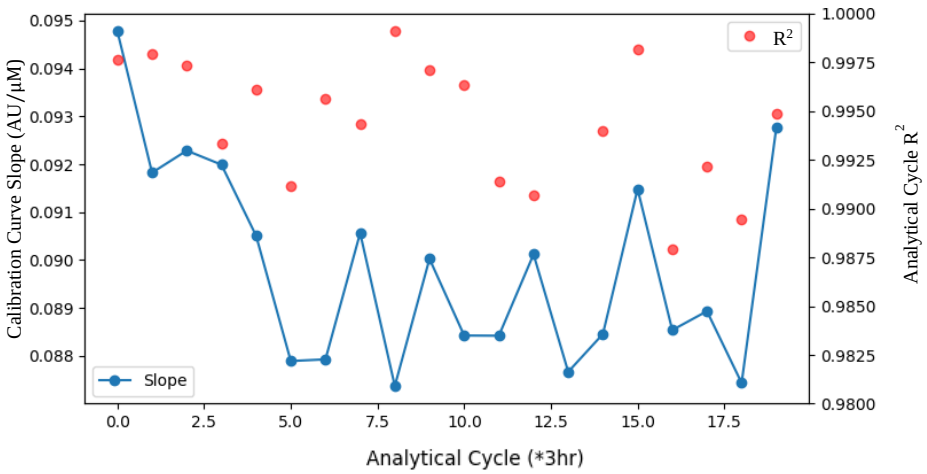

Figure 37: H_2SO_4-SDS method stability test calibration curves data

Calibration curve slopes (blue, left axis) and corresponding R^2 (red, right axis) values for each analytical cycle of the H_2SO_4-SDS method stability test. Absorbance values calculated using a 410sec reaction window with a 710nm reaction wavelength and a reference wavelength of 515nm. Note that the X-axis is the analytical cycle # over the full test length with an analytical cycle performed every 3hrs.

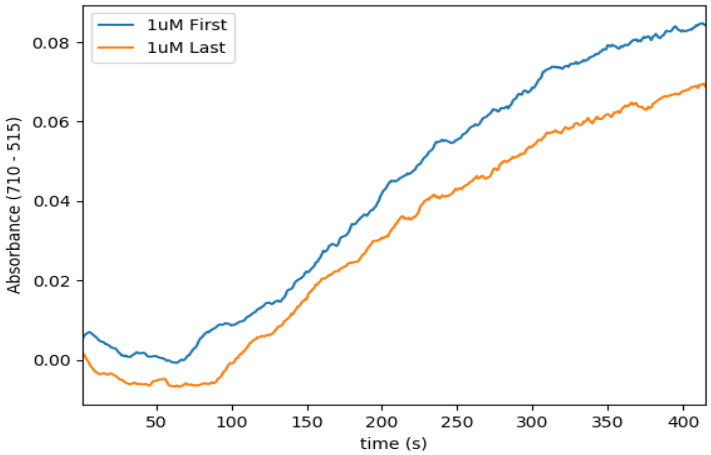

Figure 38: Beginning and ending H_2SO_4-SDS method stability test reaction curves

First and last 1.0µM PO_4 spiked SW standard reaction curves from the H_2SO_4-SDS method stability test. Reaction curves displayed over a 410sec reaction time with a 710nm reaction wavelength and a reference wavelength of 515nm.

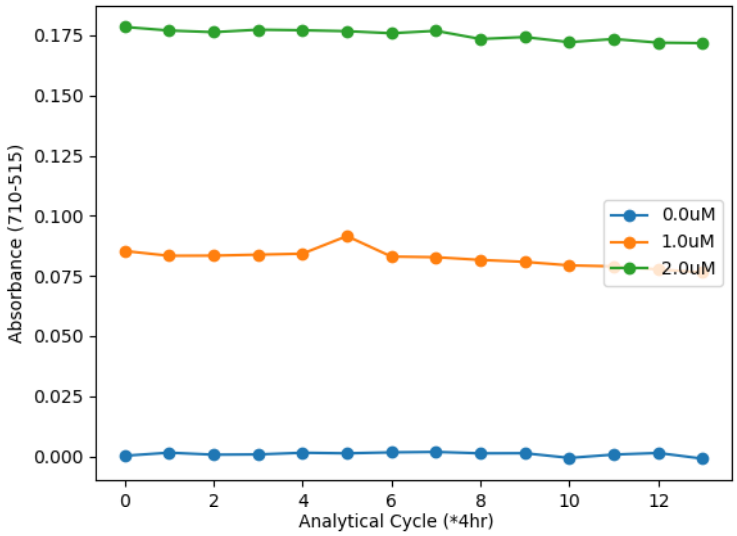

Figure 39: HCl-SDS method stability test absorbance values

Absorbance values for each standards determination sequence for the HCl-SDS method stability test. Absorbance values calculated using a 200sec reaction window with a 710nm reaction wavelength and a reference wavelength of 515nm. Note that the X-axis is the analytical cycle # over the full test length with an analytical cycle performed every 4hrs.

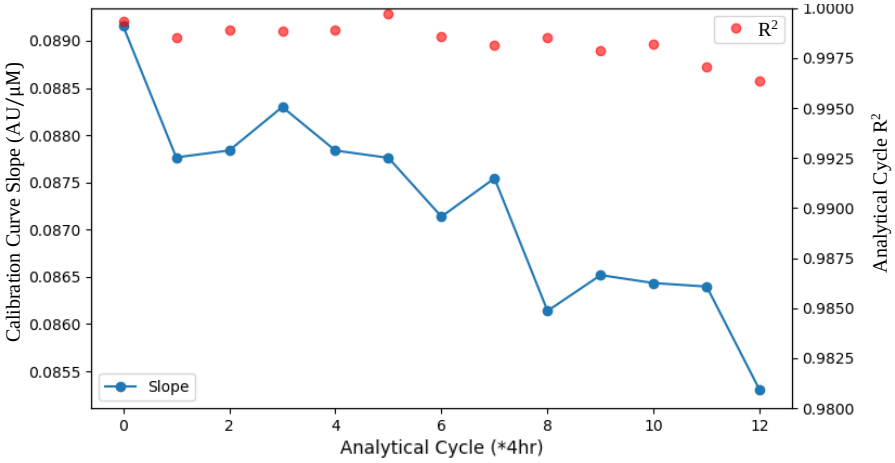

Figure 40: HCl-SDS method stability test calibration curves data

Calibration curve slopes (blue, left axis) and corresponding R^2 (red, right axis) values for each analytical cycle of the HCl-SDS method stability test. Absorbance values calculated using a 200sec reaction window with a 710nm reaction wavelength and a reference wavelength of 515nm. Note that the X-axis is the analytical cycle # over the full test length with an analytical cycle performed every 3hrs.

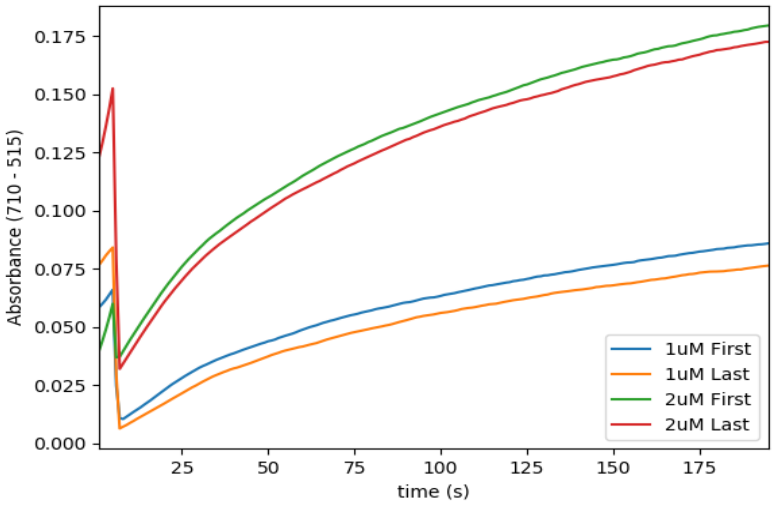

Figure 41: Beginning and ending HCl-SDS method stability test reaction curves

First and last 1.0 and 2.0µM PO_4 spiked SW standard reaction curves from the HCl-SDS method stability test. Reaction curves displayed over a 200sec reaction time with a 710nm reaction wavelength and a reference wavelength of 515nm.

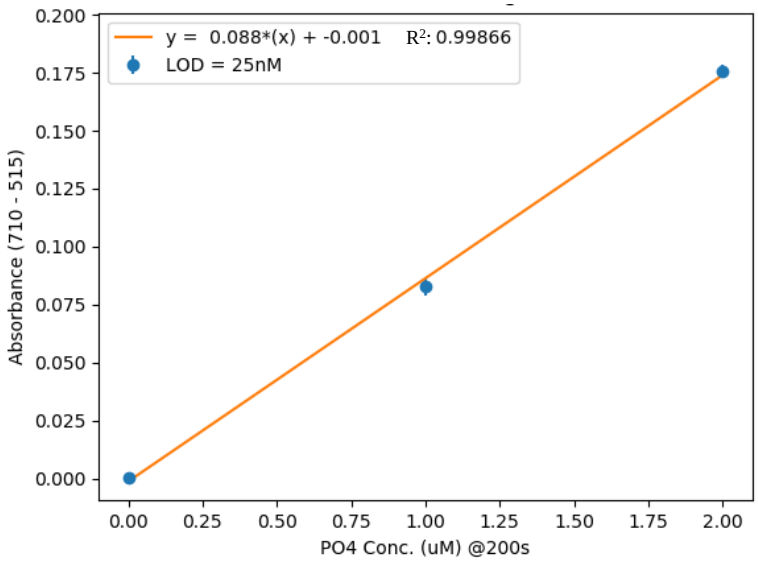

Figure 42: Full HCl-SDS method stability test averaged calibration curve

HCl-SDS calibration curve using PO_4(µM) spiked SW standards (n=12 for each point, error bars included) produced by averaging all analytical cycle across the HCl-SDS method stability test. Absorbance values calculated using a 200sec reaction window with a 710nm reaction wavelength and a reference wavelength of 515nm.

Figure 43: Map of Hawaii Kai marine embayment, Oahu, Hawaii.

Map of Hawaii Kai marine embayment, Oahu, Hawaii. The location of the dock deployment is displayed with a red marker. Image courtesy of Google Earth.

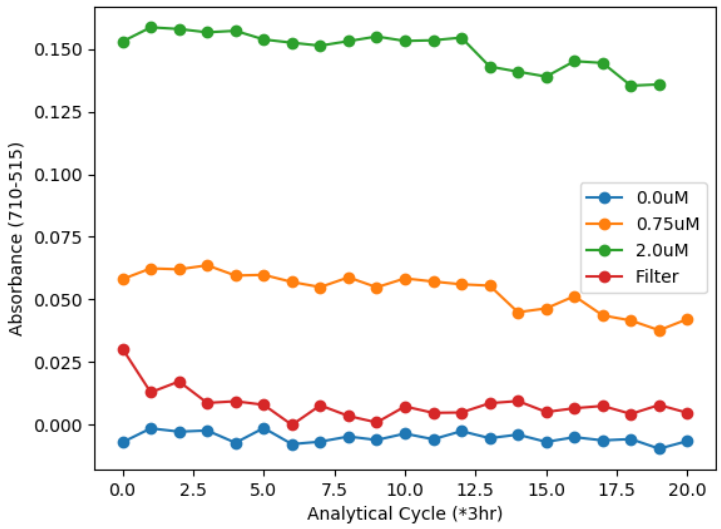

Figure 44: Dock deployment absorbance values

Determination sequence absorbance values for 0.0(blue), 0.75(orange), and 2.0µM(green) PO_4 spiked SW standards and filtered sample (red) during each analytical cycle during the dock deployment. A 600sec reaction time and 515nm reference wavelength was used. Absorbance values calculated using the H_2SO_4-SDS method with a 600sec reaction window using a 710nm reaction wavelength and a reference wavelength of 515nm. Note that the X-axis is the analytical cycle # with an analytical cycle performed every 3hrs.

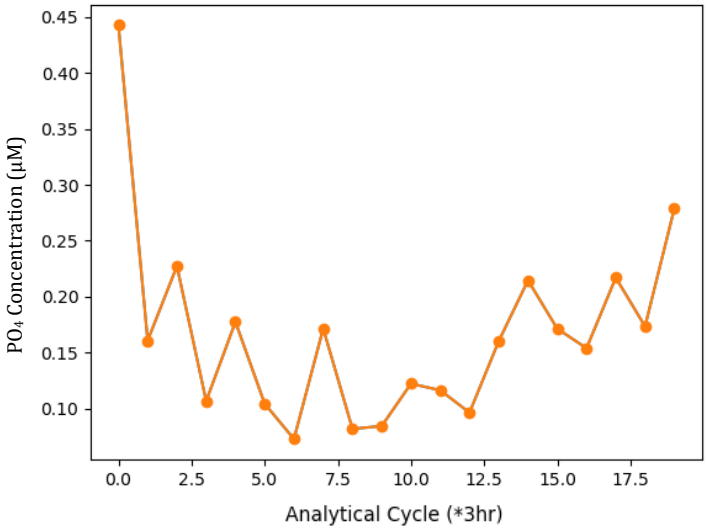

Figure 45: Dock deployment calculated filter PO_4 concentrations

Calculated PO_4 concentrations using the calibration curve produced from each analytical cycle during the dock deployment. Absorbance values calculated using the H_2SO_4-SDS method with a 600sec reaction window using a 710nm reaction wavelength and a reference wavelength of 515nm. Note that the X-axis is the analytical cycle # with an analytical cycle performed every 3hrs.

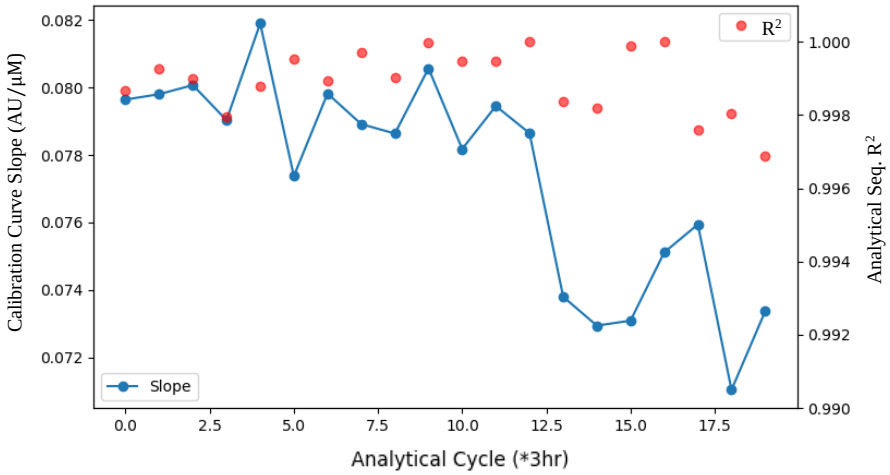

Figure 46: Dock deployment calibration curves data

Calibration curve slopes (blue, left axis) and corresponding R^2 (red, right axis) values for each analytical cycle of the dock deployment using the H_2SO_4-SDS method. Absorbance values calculated using a 600sec reaction window with a 710nm reaction wavelength and a reference wavelength of 515nm. Note that the X-axis is the analytical cycle # over the full test length with an analytical cycle performed every 3hrs.

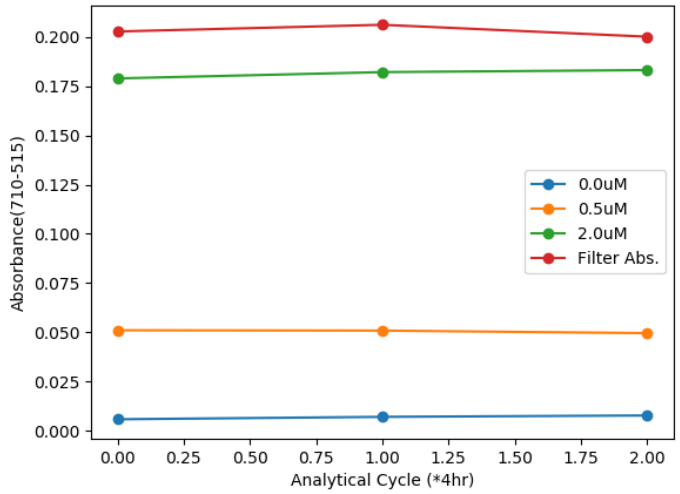

Figure 47: Submergence test absorbance data

Determination sequence absorbance values for 0.0(blue), 0.5(orange), 2.0µM(green) PO_4 spiked SW standards and an unfiltered 2.25µM sample (red) for each analytical cycle of the submergence test. Absorbance values calculated using a 200sec reaction window with a 710nm reaction wavelength and a reference wavelength of 515nm. Note that the X-axis is the analytical cycle # over the full test length with an analytical cycle performed every 4hrs.

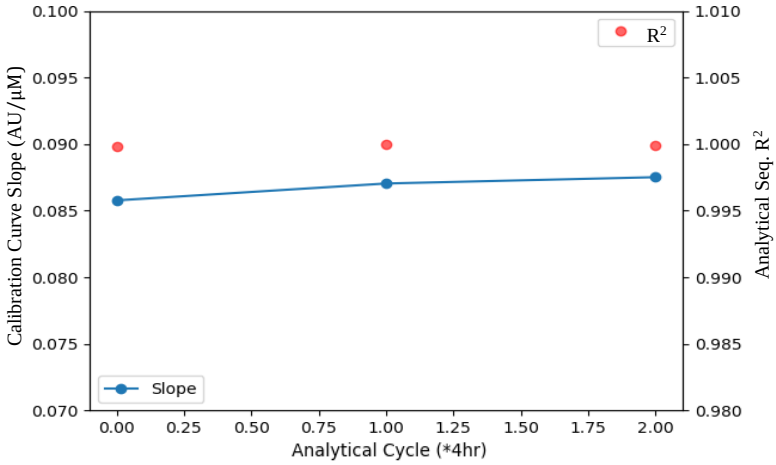

Figure 48: Submergence test calibration curves data

Calibration curve slopes (blue, left axis) and corresponding R^2 (red, right axis) values for each analytical cycle of the HCl-SDS method stability test. Absorbance values calculated using a 200sec reaction window with a 710nm reaction wavelength and a reference wavelength of 515nm. Note that the X-axis is the analytical sequence number over the full test length with an analytical cycle performed every 4hrs.

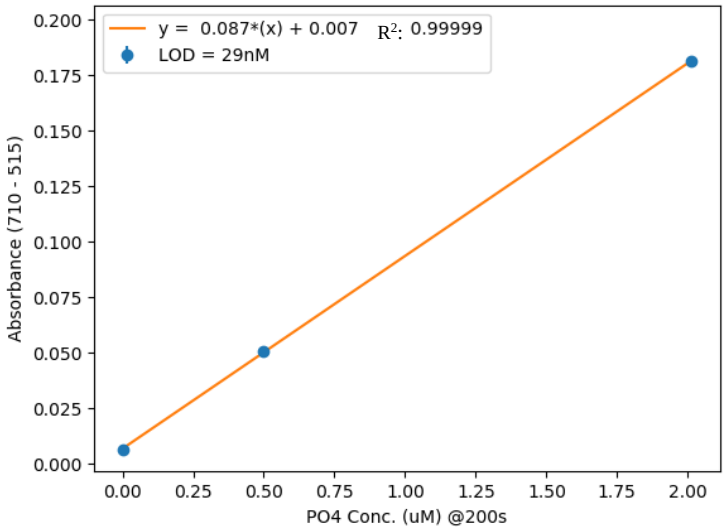

Figure 49: Full submergence test averaged calibration curve

HCl-SDS calibration curve using PO_4(µM) spiked SW standards (n=3 for each point) produced by averaging all analytical cycles across the full submergence test. Absorbance values calculated using a 200sec reaction window with a 710nm reaction wavelength and a reference wavelength of 515nm.

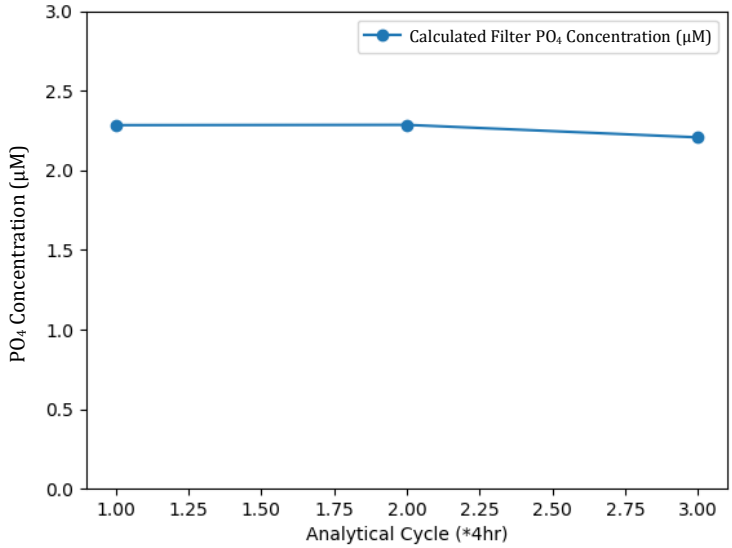

Figure 50: Submergence test calculated filter PO_4 concentrations

Calculated PO_4 concentrations using the calibration curve produced from each analytical cycle during the submergence test. Absorbance values calculated using the HCl-SDS method with a 200sec reaction window with a 710nm reaction wavelength and a reference wavelength of 515nm. Note that the X-axis is the analytical cycle # with an analytical cycle performed every 4hrs.

Figure 51: Ala Wai Offshore Observatory

Ala Wai Offshore Observatory prior to installation. The auto-sampler was attached to an upright pole, center structure, flat cross bar, and circular support.

Appendix 1. Program

```
#!/usr/bin/env python3
# -*- coding: utf-8 -*-
"""

@author: Nathaniel Harmon
"""



# Import python modules
import seabreeze
import numpy as np
import os
import pandas as pd
from math import log10
from serial import Serial
import time
import datetime
import seabreeze.spectrometers as sb



# General Variables
seabreeze.use('pyseabreeze')
devices = sb.list_devices()
spec = sb.Spectrometer(devices[0])
serv = serial.Serial(LoV_path_to_serial_port, baud_rate, timeout)
serv2 = serial.Serial(selectorValve_path_to_serial_port, baud_rate, timeout)
serp = serial.Serial(pump_path_to_serial_port, baud_rate, timeout)
spec.integration_time_micros(set_integration_time_in_microsec)

def pumpMethod(strLine, endLine, rxnTime, pushVol):
    '''
        Main method called with:
            line to start analytical sequence with: strLine = int
            line to end analytical sequence with + 1: endLine = int
```

```
        the reaction time: rxnTime = int
        volume to push reaction mixture into flow cell: pushVol = int(uL)

    Can be called from command line or added to cronjob

    proceeds from strLine to endLine
    saves pickled pandas DataFrame

    ex. pumpMethod(1, 5, 250, 155)
        runs deterimination sequence from line 1 to line 4
        rxnTime = 250sec
        pushVol 155uL

  '''

  for curline in range (strLine, endLine):
    fullFlush('waste', 1800)
    fullFlush('fc', 1200)
    analytePrime(curline)
    reagentPrime()
    baselineList = baseline(curline)
    holdingCoilLoad(curline)
    reactionList = analyze( rxnTime, pushVol)
    determinationSequence = pd.concat([ baselineList, reactionList], axis = 1)
    determinationSequence.to_pickle(path_to_directory/file_Name.pkl)
    fullFlush('fc')
    if curline != 1:
      selectorVal(5)
    fullFlush('sampVal')
    if curline == 1:
      degasClean()


def pump (direction, speed, position):
  '''
    Direction: 1 = from DI, 0 = Towards LoV
    Speed is given by stroke[] in sec/stroke (ex. 1 = 1.3sec/stroke)
```

```
        Position is absolute position from 0(empty) to 3000(full 1mL in syringe)

    '''

    stroke = [1.25,1.3,1.39,1.52,1.71,1.97,2.37,2.77,3.03,3.36,3.77,
            4.30,5,6,7.5,10,15,30,31.58,33.33,35.29,37.50,40,42.86,
            46.15,50,54.55,60,66.67,75,85.71,100]
    serp.open()
    serp.write ('/1?\r')
    s = serp.read(10)
    st = (position - int(float(s[3:-3])))
    if direction == 1:
        pumpdir = 'O'
    else:
        pumpdir = 'I'
    serp.write('1S%i%sA%sR\r' %(speed, pumpdir, position))
    strokeSpeed = stroke[speed]
    timeWait = (strokeSpeed/2) * 0.001 * abs(st)
    time.sleep(float(timeWait))
    serp.close()

def LoV (position):
    '''
    Select which Lab on Valve position as a string
    '''

    currentValPos = {'degas': '01', 'fc': '02', 'AA' : '03', 'sampVal': '04',
        'waste': '05', 'MO': '06'}
    serv.write('GO%s' %(currentValPos[str(position)]) + '\r')
    time.sleep(1)

def selectorVal(position):
    '''
        Select which Selector Valve Position as int
    '''

    currentValPos = {1: '01', 2: '02', 3: '03', 4 : '04', 5: '05',
```

```
        6: '05', 7: '06', 8: '08'}
    serv2.write('GO%s' %(currentValPos[position]) + '\r')
    time.sleep(1)

def fullFlush( line, totVol = 3000):
    '''
        flushes holding coil to line as a string
        flushes 1mL unless explicitly stated by totVol
    '''

    LoV(line)
    pump(1, 13, totVol)
    pump(0, 13, 0)

def reagentPrime():
    '''
       Primes Reagents
    '''

    pump(1, 15, 900)
    LoV('AA')
    pump(0, 15, 990)
    LoV('waste')
    pump(1, 15, 0)
    pump(1, 15, 900)
    LoV('MO')
    pump(0, 15, 990)
    LoV('waste')
    pump(1, 15, 0)

def degasFlush():
    '''
        Flushes the degas fitting on LoV
    '''

    LoV('degas')
    pump(0, 15, 3000)
```

```
    LoV('waste')
    pump(0, 15, 0)
    LoV('degas')
    pump(0, 15, 3000)
    LoV('waste')
    pump(0, 15, 0)
    fullFlush('waste')

def analytePrime(curline):
    '''
        Primes the lines between the Selector Valve and LoV
        If the curline = 1 primes the in-line filter probe
    '''

    if curline == 1:
        filtLinePrime(curline)
    else:
        stdPrime(curline)

def filtLinePrime(curline):
    '''
       Primes a filtered sample for analysis
    '''

    LoV('sampVal')
    selectorVal(curline)
    pump(0, 25, 1500)
    pump(0, 13, 3000)
    LoV('waste')
    pump(0, 15, 0)
    LoV('sampVal')
    pump(0, 25, 2700)
    LoV('degas')
    pump(0, 15, 0)
    fullFlush('waste')
    pump(0, 25, 2700)
    LoV('degas')
```

```
    pump(0, 15, 0)
    LoV('degas')
    fullFlush('waste')
    Lov('degas')
    pump(0, 15, 1800)

def stdPrime(curline):
    '''
        Primes a standard for analysis
    '''

    selectorVal(curline)
    LoV('sampVal')
    pump(0, 15, 900)
    fullFlush('waste')

def baseline(curline, list):
    '''
        Loads the flow cell with sample/standard
        takes 100 light intensity spectrums
        builds and returns pandas dataframe obj
        index = wavelength
        columns = spectrum #
    '''

    columns = np.arrange(1, 101, 1)
    intensityList = []
    index = spec.wavelengths()
    if curline == 1:
        LoV('degas')
    else:
        LoV('sampVal')
    pump(0, 15, 1800)
    LoV('fc')
    pump(0, 15, 900)
    for i in range(100):
        intensityList.append([spec.intensities(correct_dark_counts=True,\
```

```
                                        correct_nonlinearity=True)])
    df = pd.DataFrame( intensityList, index = index, columns = columns)
    return df

def holdingCoilLoad(curline):
    '''
        loads the holding coil with the reaction mixture
    '''

    pump(1, 15, 2025)
    LoV('MO')
    pump(0, 20, 2325)
    LoV('AA')
    pump(0, 20, 2475)
    if curline == 1:
        LoV('degas')
    else:
        LoV('sampVal')
    pump(0, 20, 3000)

 def analyze(rxnTime, pushVol):
    '''
        moves the reaction mixture pushVol(given in uL) into flow cell
        record light intensity spectrums for rxnTime (int)
        record time light intensity spectrum was taken
        builds and returns pandas DataFrame obj.
        index = wavelengths
        columns = time of each spectrum
    '''

    LoV('fc')
    pushVol = 3000 - (pushVol * 3)
    pump(0, 25, pushVol)
    intensityList = []
    columns = []
    index = spec.wavelengths()
    tend = time.time() + rxnTime
```

```
    start_time = time.time ()
    while time.time() < tend:
        times.append(( time.time() - start_time))
        intensityList.append([ spec.intensities( correct_dark_counts = True,\
                                correct_nonlinearity = True)])
    df = pd.DataFrame( intensityList, index= index, columns= columns)
    return df


def degasClean():
    '''
        cleans up the degas fitting
    '''

    LoV('degas')
    pump(0, 15, 2100)
    pump(1, 15, 3000)
    LoV('waste')
    pump(0, 13, 0)
    fullFlush('waste')
    fullFlush('degas')
    fullFlush('degas', totVol = 2700)
```

References

Anchor QEA, L. P. (2011). *Hawaii kai marina and entrance channel maintenance Dredging*. Retrieved from http://oeqc2.doh.hawaii.gov/EA_EIS_Library/2011-06-23-OA-FEA-Hawaii-Kai-Marina-Dredging.pdf

Barkley, A.E., Prospero, J.M., Mahowald, N., Hamilton, D.S., Popendorf, K.J., Oehlert, A.M., Pourmand, A., Gatineau, A., Panechou-Pulcherie, K., Blackwelder, P. and Gaston, C.J., 2019. African biomass burning is a substantial source of phosphorus deposition to the Amazon, Tropical Atlantic Ocean, and Southern Ocean. *Proceedings of the National Academy of Sciences*, 116(33), pp.16216-16221.

Benitez-Nelson, C. (2015). Ocean chemistry. The missing link in oceanic phosphorus cycling? *Science (New York, N.Y.), 348*(6236), 759. doi:10.1126/science.aab2801

Berner, R. A. (1973). Phosphate removal from sea water by adsorption on volcanogenic ferric oxides. *Earth and Planetary Science Letters, 18*(1), 77-86.

Berner, R. A., & Rao, J. L. (1994). Phosphorus in sediments of the amazon river and estuary - implications for the global flux of phosphorus to the sea. *Geochimica Et Cosmochimica Acta, 58*(10), 2333-2339.

Burnett, W. C. (1977). Geochemistry and origin of phosphorite deposits from off Peru and Chile. *Geological Society of America Bulletin, 88*(6), 813-7606-7688-7606-7813-17427.

Caraco, N. (1995). Influence of human populations on phosphorus transfers to aquatic systems: a regional scale study using large rivers. *Scope-Scientific Committee On Problems Of The Environment International Council Of Scientific Unions, 54*, 235-244.

Cavender-Bares, K. K., Karl, D. M., & Chisholm, S. W. (2001). Nutrient gradients in the western North Atlantic Ocean: Relationship to microbial community structure and comparison to patterns in the Pacific Ocean. *Deep Sea Research Part I: Oceanographic Research Papers, 48*(11), 2373-2395.

Colman, A.S. and Holland, H.D. (1994) Benthic phosphorus regeneration: The global diffusive flux of phosphorus from marine sediments into the oceans. *EOS Transactions, American Geophysical Union* 75: 96.

Compton, J., Mallinson, D., Glenn, C.R., Filippelli, G., Föllmi, K., Shields, G. and Zanin, Y., 2000. Variations in the global phosphorus cycle. In: Glenn C.R., Pre´voˆt-Lucas L., and Lucas J. (eds.) Marine Authigenesis: From Global to Microbial, pp. 21–33. Oklahoma: SEPM. Special Publication #66.

Cordell, D. (2010). The Story of Phosphorus: Sustainability implications of global phosphorus scarcity for food security: Långsiktig inverkan av fosforbrist på global matsäkerhet. In.

Crosby, S. A., Millward, G. E., Butler, E. I., Turner, D. R., & Whitfield, M. (1984). Kinetics of phosphate adsorption by iron oxyhydroxides in aqueous systems. *Estuarine Coastal and Shelf Science, 19*(2), 257-270.

Dregne, H. E. (2002). Land Degradation in the Drylands. *Arid Land Research and Management, 16*(2), 99-132.

Duce, R.A., Liss, P.S., Merrill, J.T., Atlas, E.L., Buat‐Menard, P., Hicks, B.B., Miller, J.M., Prospero, J.M., Arimoto, R.C.T.M., Church, T.M. and Ellis, W., 1991. The atmospheric

input of trace species to the world ocean. *Global Biogeochemical Cycles*, 5(3), pp.193-259.

El-Sayed, A.Y., Hussein, Y. Z., & Mohammed, M. A. (2001). Simultaneous determination of phosphate and silicate by first-derivative spectrophotometry. *Analytical sciences, 17*(12), 1461-1464.

Elser, J. J. (2012). Phosphorus: a limiting nutrient for humanity? *Current Opinion in Biotechnology, 23*(6), 833-838. doi:10.1016/j.copbio.2012.03.001

Erisman, J. W., Galloway, J. N., Seitzinger, S., Bleeker, A., Dise, N. B., Petrescu, A. R., Leach, A.M., de Vries, W. (2013). Consequences of Human Modification of the Global Nitrogen Cycle. *Philosophical Transactions of the Royal Society B: Biological Sciences, 368*(1621), 20130116.

Fontaine, T. (1942). Spectrophotometric Determination of Phosphorus. *Industrial & Engineering Chemistry Analytical Edition, 14*(1), 77-78.

Fox, L. E. (1990). Geochemistry of Dissolved Phosphate in the Sepik River and Estuary, Papua, New-Guinea. *Geochimica Et Cosmochimica Acta, 54*(4), 1019-1024.

Guidry, M. W., & Mackenzie, F. T. (2000). Apatite weathering and the Phanerozoic phosphorus cycle. *Geology, 28*(7), 631-634.

Harris, W., & Popat, P. (1954). Determination of the phosphorus content of lipids. *Journal of the American Oil Chemists' Society, 31*(4), 124-127.

Hatta, M., Measures, C. I., & Ruzicka, J. (2018). *Phosphate determination using micro-Sequential Injection Lab on Valve during an international nutrient inter-calibration cruise in the Southern Ocean.* Paper presented at the Ocean Sciences, Portland, OR.

Hatta, M., Measures, C. I., & Ruzicka, J. J. (2019). Determination of traces of phosphate in sea water automated by programmable flow injection: Surfactant enhancement of the phosphomolybdenum blue response. *Talanta, 191*, 333.

Hecky, R. E., & Kilham, P. (1988). Nutrient limitation of phytoplankton in fresh-water and marine environments - a review of recent-evidence on the effects of enrichment. *Limnology and Oceanography, 33*(4), 796-822.

Hesse, G., & Geller, K. (1968). Phosphorus (nucleotide phosphorus) determination with a stannous chloride hydrazine sulfate reagent by the Hurst method. *Mikrochim. Acta*, 526-533.

Hoover, D.J., Mackenzie, F.T. Fluvial Fluxes of Water, Suspended Particulate Matter, and Nutrients and Potential Impacts on Tropical Coastal Water Biogeochemistry: Oahu, *Hawai'i. Aquat Geochem* 15, 547–570 (2009).

Howarth R.W., Jensen H.S., Marino R., and Postma H. (1995) Transport to and processing of P in near-shore and oceanic waters. In: Tiessen H. (ed.) Phosphorus in the Global Environment, ch. 19, pp. 323–345. Chichester: Wiley. SCOPE 54.

Jahnke, R.A. (1992) The phosphorus cycle. In: Butcher SS, Charlson RJ, Orians GH, and Wolff GV (eds.) Global Geochemical Cycles, ch. 14, pp. 301–315. San Diego: Academic.

Keggin, J. F. (1934). The Structure and Formula of 12-Phosphotungstic Acid. Proceedings of the Royal Society of London. Series A, Containing Papers of a Mathematical and Physical Character, 144(851), 75-100.

Kirby, A. J., & Warren, S. G. (1967). The organic chemistry of phosphorus (Vol. 1): Elsevier Pub. Co.

Kriss, E., Rudenko, V., & Yatsimirskii, K. (1971). Reduction of molybdate to molybdenum blue by various reducing agents. *Zh. Neorg. Chim, 16*(2147), e2153.

Lamond, A. I. (2002). Molecular biology of the cell, 4th edition. *Nature, 417*(6887), 383-383.

Lerman A, Mackenzie FT, and Garrels RM (1975) Modeling of geochemical cycles: Phosphorus as an example. G*eological Society of America Memoir* 142: 205–217.

Lundgren, D. P. (1960). Phosphate Analysis with Technicon AutoAnalyzer. Selective Orthophosphate and Total Inorganic Phosphate Determinations. *Analytical Chemistry*, 32(7), 824-828.

Mackenzie, F., De Carlo, E., & Lerman, A. (2011). 5.10-Coupled C, N, P, and O Biogeochemical Cycling at the Land–Ocean Interface. *Treatise on estuarine and coastal science*, 317-342.

Mackenzie, F. & Tanaka, K.. (2005). Ecosystem behavior of southern Kaneohe Bay: A statistical and modeling approach. *Ecological Modeling*. v. 188. pp. 296-326.

Mackenzie FT, Ver LM, Sabine C, Lane M, and Lerman A (1993) C, N, P, S Global biogeochemical cycles and modeling of global change. In: Wollast R, Mackenzie FT, and Chou L (eds.) Interactions of C, N, P and S Biogeochemical Cycles and Global Change. NATO ASI Series 1, vol. 4, pp. 1–61. Berlin: Springer-Verlag.

Mackenzie, F. T., Ver, L. M., & Lerman, A. (2002). Century-scale nitrogen and phosphorus controls of the carbon cycle. *Chemical Geology, 190*(1), 13-32.

Meybeck, M. (1982). Carbon, nitrogen, and phosphorus transport by world rivers. *American Journal of Science, 282*(4), 401-450.

Moore, W. S. (2010). The Effect of Submarine Groundwater Discharge on the Ocean. In *Annual Review of Marine Science* (Vol. 2, pp. 59-88). Palo Alto: Annual Reviews.

Murphy, J., & Riley, J. P. (1962). A modified single solution method for the determination of phosphate in natural waters. *Analytica Chimica Acta*, 27(C), 31-36.

Müller, A., & Serain, C. (2000). Soluble molybdenum blues-"des Pudels Kern". *Accounts of chemical research,* 33(1), 2.

Nagul, E.A., Fontas, C., McKelvie, I.D., Cattrall, R.W. and Kolev, S.D., (2013). The use of a polymer inclusion membrane for on-line separation and preconcentration of dissolved reactive phosphorus. *Analytica Chimica Acta*, 803, pp.82-90.

Nagul, E. A., McKelvie, I. D., Worsfold, P., & Kolev, S. D. (2015). The molybdenum blue reaction for the determination of orthophosphate revisited: Opening the black box. Analytica Chimica Acta, 890, 60-82.

Paytan, A., & McLaughlin, K. (2007). The oceanic phosphorus cycle. *Chemical Reviews, 107*(2), 563-576.

Post, W. M., Peng, T.-H., Emanuel, W. R., King, A. W., Dale, V. H., & DeAngelis, D. L. (1990). The global carbon cycle. *American scientist, 78*(4), 310-326.

Redfield, A. C. (1958). The biological control of chemical factors in the environment. *American Scientist, 46*(3), 230A-221.

Richey JE (1983) The phosphorus cycle. In: Bolin B and Cook RB (eds.) The Major Biogeochemical Cycles and Their Interactions, pp. 51–56. Chichester: John Wiley and Sons. SCOPE 21.

Ringuet, S., & Mackenzie, F. T. (2005). Controls on nutrient and phytoplankton dynamics during normal flow and storm runoff conditions, southern Kaneohe Bay, Hawaii. Estuaries, 28(3), 327-337.

Ruttenberg, K. C. (2014). *10.13 - The Global Phosphorus Cycle*: Elsevier Ltd.
Ruttenberg KC and Berner RA (1993) Authigenic apatite formation and burial in sediments from non-upwelling continental margins. *Geochimica et Cosmochimica Acta* 57: 991–1007.
Ruzicka, J. Flow Injection Tutorial. Retrieved 2019 from http://www.flowinjectiontutorial.com
Ruzicka, J. (2016). From continuous flow analysis to programmable Flow Injection techniques. A history and tutorial of emerging methodologies. *Talanta, 158*, 299-305.
Ruzicka, J., & Hansen, E. H. (1975). Flow injection analyses: Part I. A new concept of fast continuous flow analysis. *Analytica Chimica Acta, 78*(1), 145-157.
Ruzicka, J., & Marshall, G. D. (1990). Sequential injection: a new concept for chemical sensors, process analysis and laboratory assays. *Analytica Chimica Acta*, 237(C), 329-343.
Ruzicka, J., Marshall, G. D., Measures, C. I., & Hatta, M. (2019). Flow injection programmed to function in batch mode is used to determine molar absorptivity and to investigate the phosphomolybdenum blue method. *Talanta, 201*, 519-526.
Ruzicka, J., & Stewart, J. W. B. (1975). Flow injection analysis: Part II. Ultrafast determination of phosphorus in plant material by continuous flow spectrophotometry. *Analytica Chimica Acta*, 79(C), 79-91.
Sims, R. (1961). Formation of heteropoly blue by some reduction procedures used in the micro-determination of phosphorus. *Analyst, 86*(1026), 584-590.
Skeggs, L. T. (1957). An automatic method for colorimetric analysis. *American Journal Of Clinical Pathology*, 28(3), 311.
Sverdrup, H. U., Johnson, M. W., & Fleming, R. H. (1942). *The Oceans: Their Physics, Chemistry, And General Biology* (Vol. 7). New York: Prentice-Hall.
Wheat CG, McManus J, Mottl MJ, and Giambalvo E (2003) Oceanic phosphiorus imbalance: Magnitude of the mid-ocean flank hydrothermal sink. *Geophysical Research Letters* 30(17).
Worsfold, P.J., Clough, R., Lohan, M.C., Monbet, P., Ellis, P.S., Quétel, C.R., Floor, G.H. and McKelvie, I.D., 2013. Flow injection analysis as a tool for enhancing oceanographic nutrient measurements—A review. Analytica Chimica Acta, 803, pp.15-40.